Examination of Premixed Methane Air Tubular Flame Response to Elevated Pressure

By

Marsalis Patrick Pullen

Thesis
Submitted to the Faculty of the
Graduate School of Vanderbilt University
In partial fulfillment of the requirements
For the degree of

MASTER OF SCIENCE
in
Mechanical Engineering

May 14, 2021

Nashville, Tennessee

Approved:

Robert W. Pitz, Ph.D.

Haoxiang Luo, Ph.D.

Carl Hall, Ph.D.

ACKNOWLEDGEMENTS

> No man is an island entire of itself; every man
> is a piece of the continent, a part of the main;
> if a clod be washed away by the sea, Europe
> is the less, as well as if a promontory were, as
> well as any manner of thy friends or of thine
> own were; any man's death diminishes me,
> because I am involved in mankind.
> And therefore never send to know for whom
> the bell tolls; it tolls for thee.
>
> John Donne (1572 -1631)

Firstly, I would like to express my sincere gratitude to my advisor, Dr. Robert Pitz, for the continuous support of my academic study and related research, for his patience, motivation, and immense knowledge. His guidance helped me in all the time of research and writing of this thesis. I could not have imagined having a better advisor and mentor for my work.

I would also like to thank Dr. Haoxing Luo and Dr. Carl Hall for their insightful comments and encouragement. I wholeheartedly appreciate your great advice and support in my academic endeavours.

The physical and technical contributions of the American Chemical Society and King Abdullah University of Science and Technology, specifically Dr. Bill Roberts and the Clean Combustion Research Center is truly appreciated. Without their support and funding, this project could not have reached its goal.

I wish to acknowledge the support and great love of my family, my wife, Hanna Fonataba; my mother, Pamela; my father, Robert; and my brothers, Brandon and Jordan. They kept supporting me throughout writing this thesis and life in general.

Gratitude extends to Darren Tinker, Harshinin Devathi, Garrett Marshall, Chad Carpenter, and Conrad Reihsmann for the stimulating discussions, for the invaluable assistance that you all provided, and for all the fun we have had in the last three years. I also thank my friends from Tennessee Technological University. In particular, I am grateful to Dr. Stephen Idem for enlightening me on the first glance of research.

TABLE OF CONTENTS

LIST OF FIGURES

LIST OF TABLES

NOMENCLATURE

Greek

α	Thermal diffusivity
μ	Mixture viscosity
ν	Kinematic viscosity
ν_f	Frequency
ϕ	Equivalence Ratio
σ	Stefan-Boltzmann constant
τ_c	Chemical Reaction Time
τ_m	Fluid Flow Time
θ	Tangential Coordinate

EnglishOQSubscripts and Superscripts

$\overrightarrow{u}$	Velocity field
$\tilde{p}_1$	Perturbed pressure field
h_p	Planck's constant
N_c	Number of flame cells
Q_{rad}	Radiation heat loss
u_θ	Tangential velocity component
u_r	Radial velocity component
u_z	Axial velocity component
A	Area
D	Mass diffusion coefficient
D$_h$	Outer nozzle exit height (8 mm)
Da	Damköhler number
H	Pressure eigenvalue
I	Radial and Azimuthal pressure
k	Stretch rate
Le	Lewis Number
R	Outer nozzle radius (12 mm)
r	Radial Coordinate
Re	Reynolds Number

S	Set of chemical species
T	Temperature
t	Time
W	Axial velocity gradient
X	Mole fraction
Y	Mass fraction
z	Axial Coordinate

Acronyms

BC	Boundary Condition
CCRC	Clean Combustion Research Center
DNS	Direct Numerical Simulation
HPCD	High Pressure Combustion Duct
KAUST	King Abdullah University of Science and Technology
PIV	Particle Imaging Velocimetry

Subscripts and Superscripts

i	Species number
j	Index number unless otherwise stated
st	Stoichiometric conditions

Chapter I

INTRODUCTION

Fossil fuels are a global power source, and will remain the primary form of energy in the decades to come. Combustion is critical to countless applications in energy production and conversion, benefiting societal welfare for decades through the development of various compact and robust devices. The accurate control of turbulent flames in these devices is a prevailing challenge. In turbulent combustion, flames possess characteristics that make it difficult for current computational resources to simulate accurately and efficiently in full detail. Full-scale systems are mandatory to experimentally examine the interaction between the turbulent flow, chemical kinetics, mass and energy transfer, and flame instabilities. It is ubiquitous to reduce the complexity of these reacting flows by studying flames at an elementary level.

Turbulent flames have been shown to be an ensemble of stretched laminar flamelets [1, 2]. This idea has led to the development of the laminar flamelet model. The model takes into account that the reaction zone for flames are very thin and turbulent flow yields similar effects to laminar flame structure under the same dissipation rate [3]. Laminar flames are computationally and experimentally inexpensive for comparison and evaluation of chemical mechanisms and transport phenomena in turbulent flames. It is through in-depth laminar flame studies that current turbulent modeling can be improved upon, which will provide more insight into combustion phenomena.

Laminar studies utilize various types of burners that produce unique flame geometries based on the configuration of the inlet nozzles and stagnation point. Two similar types of burners are axially [4] and radially [5] opposed jets as shown in the simplified schematic Figure 1.1. The flame position for a combustible, premixed mixture, is where the laminar flame velocity is equal to the local gas velocity. The velocity at the stagnation plane is zero, so the flame will be at some position away from the stagnation plane.

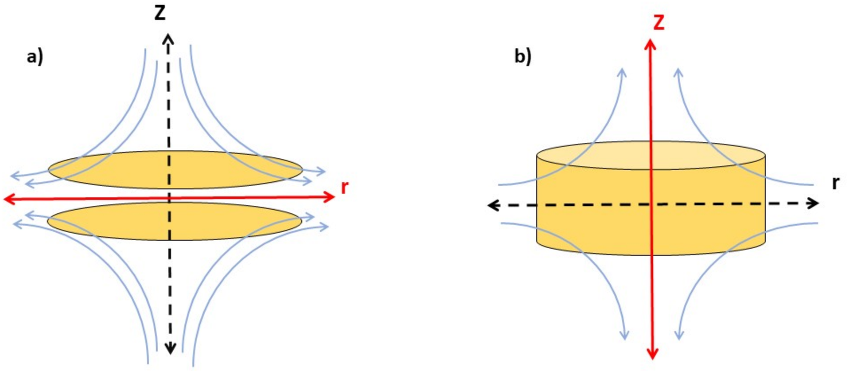

Figure 1.1: Combustible mixture (blue lines) stagnate at the radial and axial coordinate (red line) respectively. In a) the flame expands along the diverging flow and is balanced by the momentum of the two jets. In b) the flame expands and is balanced by the momentum of the incoming radial flow to form a tubular flame.

An axially opposed jet creates a thin planar flame sheet by having reactants contact axially, stagnate, and exit in the radial direction. Twin premixed flames are produced if there are premixed combustible mixtures on both sides of the stagnation plane. In this case, each flame sheet is offset from the stagnation plane. If one side is hot products and the other is a combustible mixture, then a single premixed flame will form on the combustible mixture side of the stagnation plane. Radial opposed jets create flames in a cylindrical or tubular shape by having reactants contact radially, stagnate, and exit in the axial direction.

While each configuration generates a unique structure, an axial jet is limited to observing flame stretch, whereas practical combustors produce flames that are not only stretched but also curved. It is important to examine stretch and curvature in flames since real-world combustors inherently possess both characteristics. The tubular burner has an ideal geometry as it can independently study each parameter to determine flame temperature and composition.

The goal of the present study is to perform an experimental and numerical investigation of methane-air tubular flames at elevated pressures. Methane was chosen due to its abundance in natural gas and renewed interest as a rocket fuel in aerospace engine development [6]. Experimental work involves capturing chemiluminescent images of tubular flame to examine their structure and behavior from 1 to 5 bar. In order to model tubular flames, an in-house code [7] is employed to compare reduced chemical mechanisms to predict temperature, composition, speed, radius, and thickness. With these results, the structure of high pressure tubular flames will be characterized, and the ability for more high-pressure studies to impact investigations of practical flames is examined.

1.1 Stretch Rate

The interplay between the flow field and flame structure is characterized by changes on the flame surface. This effect is known as the stretch rate, a factor also prevalent in turbulent flames introduced by Karlovitz et al [8]. It is an expansion of the flame sheet that can alter certain parameters such as species diffusivities, flame thickness, speed, and temperature. The global tubular premixed stretch rate from the flow field stagnation line is defined as,

$$k = \frac{\pi V}{R} \tag{1.1}$$

where V is the inlet velocity and R is the radius of the outer nozzle [9]. The stretch rate is also a primary cause of flame extinction [10]. Where extinction can defined as being the point where the flame extinguishes due to not being able to maintain a sustained burning rate. Radiation has been shown to be dominate parameter for extinguishment at low stretch rates (k $< 4s^{-1}$) [11]. The flame will extinguish as equivalence ratio is increased because more energy is required to account for the heat loss to the environment.

1.2 Damköhler Number

In order to expand on the physical nature of combustion, it is necessary to examine the extent of chemical reaction time on flame structure. The flame temperature is dependent on the time required for completion of reactions and the residence time of the reacting species. This effect can be characterized by the first Damköhler number,

$$Da = \frac{\tau_m}{\tau_c} \tag{1.2}$$

where τ_m is the fluid flow time and τ_c is the chemical reaction time. For Damköhler number much less than unity the chemical reaction time is longer, reducing the residence time of reactants within the flame for consumption. For Damköhler number much greater than unity the fluid flow time is longer, increasing the residence time of reactants within the flame for completion. A highly stretched tubular flame will have a thin reaction zone which decreases the residence time of the reacting species compared to the chemical time to react within the flame. It has been shown that the flame temperature and speed will increase with stretch rate for a high Damköhler number, far from extinction, and sub-unity Lewis number tubular flame [12]. It is expected that the Damköhler number will play a greater role in tubular flame temperature at elevated pressures.

1.3 Equivalence Ratio

A fundamental distinction in combustion is the difference between diffusion and premixed flames. A diffusion flame is a scenario where the fuel and oxidizer are separate during the flow process. A premixed flame is a scenario where the fuel and oxidizer are well- mixed before initiation. To quantify the chemical structure of premixed flames, a normalized ratio of the fuel-oxidizer is necessary,

$$\Phi = \frac{(\frac{X_f}{X_o})}{(\frac{X_f}{X_o})_{st}} \tag{1.3}$$

where x_f is the fuel mole fraction, x_o is the oxidizer mole fraction, and the denominator is the stoichiometric fuel-oxidizer ratio. The standard range for the equivalence ratio is sub-unity for lean flames, unity for stoichiometry, and above unity for rich flames. A diffusion flame will naturally situate itself somewhere at or near stoichiometry to maintain burning. A premixed flame; however, has a substantial degree of variance allowed for in-depth investigations of flame structure and chemistry.

1.4 Instabilities

Either by design or nature, instabilities can serve different roles in different combustion systems. Large-scale devices such as gas turbines, can be hampered or enhanced by their presence whereas at the smaller scale the instabilities can be considered an intrinsic process. It is in the smaller scale that finer details can be seen such as the formation of sharp folds, creases, or wrinkling in flame surface [13]. Instabilities in the tubular burner can typically be seen in the formation of a cellular structure. Premixed tubular flames have been found to produce cellular instabilities as a result of a thermal diffusive effect [14]. This effect can be characterized by the Lewis number (Le),

$$Le = \frac{\alpha}{D} \tag{1.4}$$

where α is the thermal diffusivity of the mixture and D is the mass diffusivity of the deficient reactant. In premixed flames, the mass diffusivity is from the deficient reactant, which corresponds to fuel in lean flames and oxidizer in rich flames.

In premixed flames, the Lewis number can impact the flame temperature through the stretch rate. This is known as preferential diffusion. When stretched, the flame is thinned. This causes the temperature and species gradients to become even more sensitive to mass and thermal diffusivities. For Lewis number less than unity the mass diffusivity of the deficient reactant is greater into the flame, increasing the temperature above adiabatic with increasing stretch rate. For Lewis number greater than unity the thermal diffusivity of the deficient reactant is greater out of the flame, reducing the temperature below adiabatic with increasing stretch rate.

In tubular flames, an instability comes in the formation of cells a result of Lewis number less than unity. According to Equation 1.4, this is a result of mass diffusion being the dominate factor over thermal transport causing local extinction to occur in the reaction zone. However, it has been shown that nearly equidiffusive (Le $\approx$ 1) flames such as premixed methane-air do not form cells at atmospheric pressure [14]. In light of this information, it is expected that even in an high-pressure environment local extinction will not occur for tubular methane-air flames.

This body of work is an attempt to address the dearth of experimental data in high-pressure premixed tubular flames. Chapter II discusses previous numerical campaigns of high-pressure tubular flames and opposed jets. Chapter III describes the high-pressure combustion duct, tubular burner, flame conditions, and in-house code used in this work. Chapter VI analyzes work on lean methane-air premixed flame response to elevated pressure. Chapters V and VI provides a summary of the work covered here and presents ideas for future work.

Chapter II

LITERATURE REVIEW

Despite the fact that extensive research has been conducted on tubular flames at atmospheric pressure for various fuels [7, 15] and configurations [5, 16, 17], literature at elevated pressures has been rare. The following studies examined tubular flame behavior only through similarity and computational models. The conclusions are compared to opposed-jet flames to understand how flame geometry can have an impact on flame properties in high-pressure environments.

Nishioka et al. [18] numerically observed the structure and extinction of stoichiometric methane-air flames from pressures ranging from 1 to 8 atmosphere(s). The authors found that the elevated pressures decrease the flame radius, speed, and thickness through the reduction of thermal and species diffusivities. These decreases in flame properties can be attributed to the pressure sensitive third order reactions such as

$$H + O_2 + M \rightarrow HO_2 + M \tag{2.1}$$

which in turn affect the chain branching mechanisms and ultimately slow the rate of energy release [19]. In addition, the decrease in thermal and species diffusivities leads to steeper temperature and concentration gradients in the flame. In high pressure, third-body reaction rates are accelerated which increases the flame temperature to an equilibrium temperature.

Zhang et al. [20] numerically compared lean ($\phi = 0.7$) methane-air opposed-jet and tubular flames from 0.5 to 3 atmosphere(s). The authors concluded that pressure variations influence the maximum flame temperature of opposed jets and tubular flames through curvature. At pressures above 1 atmosphere, the opposed flame temperature increased slightly at low stretch rate before decreasing at higher stretch rates. However, the tubular flame temperature steadily increased with increasing stretch rate. The higher stretch rates in tubular flames result in a larger flame curvature that contributes to an increase in temperature as pressure rises. Ultimately, the flame temperature depends on pressure and curvature which is the principal difference in between these flame configurations.

It is compelling to extend the discussion further by briefly mentioning the effect of pressure on opposed-jet flames. Counterflow experiments at elevated pressures have been shown to possess a different flame response, more importantly on flame thickness, speed, and temperature [21–25]. Sun et al. [26] experimentally and numerically studied high-pressure counterflow responses for both near-equidiffusive and non-equidiffusive premixed flames. For near-equidiffusive (Le = 1.01) methane-air ($\phi = 0.95$) flames, the maximum flame temperature remains unchanged across various strain rates. This illustrates the the structural insensitivity of these unity Lewis number flames to variations in pressure and strain. For non-equidiffusive (Le = 1.84 and Le = 0.93) propane-air ($\phi = 0.7$ and $\phi = 1.8$) flames, the maximum flame temperature is nearly insensitive to changes in pressure. The above unity Lewis number flames show a small decrease in maximum temperature, while sub-unity flames have a slight increase. The minor changes in maximum temperature can be attributed to the influence of stretch on the decreased flame thickness.

It is apparent from the numerical investigations on tubular flames that pressure increases flame temperature and decreases flame thickness, radius, and speed. In the experimental realm, an understanding of the characteristics and behavior of high pressure premixed tubular flames is still nonexistent. In short, due to the novelty of high-pressure tubular flames, the objectives of the research are: 1) analyze flame geometry via chemiluminescence and 2) compare simulations with previous findings on structural properties and concentrations.

Chapter III

EXPERIMENTAL APPROACH

Experimental characterizations were performed with chemiluminescence imaging, which allows for an analysis of high-pressure instabilities in tubular flame structure. This type of investigation has not been previously performed in tubular flames, most likely due to the associated risks and costs with operating a high-pressure facility. Nevertheless, experimental data of high-pressure tubular flames are imperative to develop and test computational models with detailed transport and chemistry under pressure conditions of practical systems.

3.1 High-Pressure Combustion Duct

The presented work was performed in the high-pressure combustion duct (HPCD) in the Clean Combustion Research Center (CCRC) at King Abdullah University of Science and Technology (KAUST). The HPCD, shown in Figure 3.1, is a 7.5 m long, air-cooled, 316L stainless-steel pipe (ID = 410 mm) designed to operate up to 40 bar and 250° C. The optical section of the duct consist of six windows with the tubular burner mounted on a 3-axis translation stage to allow minor adjustments for diagnostics. The HPCD has a dome-loaded back pressure regulator for adjustments, and in order to maintain a desired pressure, the co-flow air is supplied continuously to dissipate the flame's thermal power [27–29].

As stated previously, high-pressure campaigns have not be performed due to the risks and costs associated with building and maintaining such a facility. There are other problems that become apparent with operation of the tubular burner inside the HPCD.

The entire weight of the HPCD (several tons) is supported by a table that operates as an external lift to raise and lower the bottom flange containing the internal vertical translation stage. If there are any significant issues with the tubular burner during measurements, then the disassembly and reassembly time of the bottom flange section of the HPCD can take up to three days. This, coupled with the fact that other robust scientific campaigns occur within the same space, means a large portion of time can be lost when reopening the HPCD.

Speaking of time, flashback is likely to occur during experimental measurements. Flashback is a combustion phenomena that can arise from either too much fuel concentration into the flame or an imbalance of flame speed and inlet flow velocity. The resulting flashback will generate condensate on the interior surfaces of the tubular burner. This condensate must be removed immediately; otherwise, the laser energy from the ignition system can cause thermal stresses to build until an optical window breaks. A cracked optical window, while not as severe as disconnecting the bottom flange of the HPCD, can take several hours to exchange.

All of the gas connections to the inside of the HPCD are made through the bottom flange. The HPCD is often employed to make Particle Imaging Velocimetry (PIV) measurements. PIV is a non-intrusive technique for visualization and instantaneous velocity measurements by using a laser to illuminate the particles and capture the location of said particles in space. In order to perform PIV in the HPCD, these particles must be injected using one of the gas connections at the bottom flange. In this presented work, unforeseen titanium oxide particles from PIV were injected into the porous plates of the tubular burner, jeopardizing the flow uniformity.

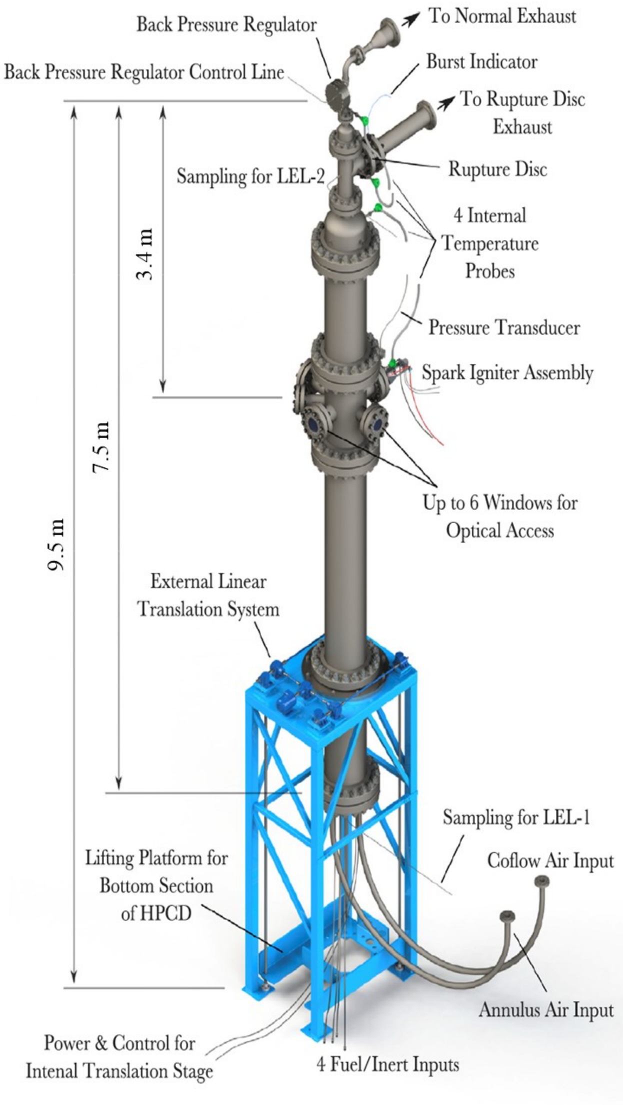

Figure 3.1: High-pressure duct located in the Clean Combustion Research Center (CCRC) at King Abdullah University of Science and Technology (KAUST) [27–29].

3.2 Tubular Burner

Vanderbilt's tubular burner has been designed for uniform, laminar flow studies [12]. A simplified schematic of the burner in premixed configuration can be seen in Figure 3.2. The gas mixture flows through annular, sintered-metal porous plates (not shown) to ensure uniform flow towards the cylindrical nozzle exit of 8 mm in height and 24 mm in diameter. There are also inert, usually N_2, co-flows situated near the nozzle exit to maintain inlet temperature and velocity. The burner possesses three optical access windows oriented 90° from each other for viewing and laser diagnostics.

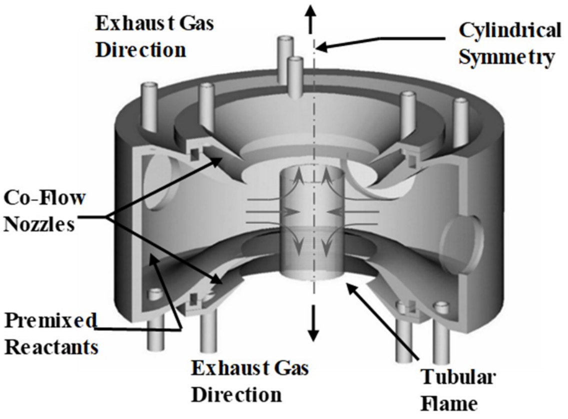

Figure 3.2: Schematic of the tubular burner.

3.3 Spark Ignition

A schematic of the spark ignition system for the High-Pressure Combustion Duct (HPCD) is shown in Figure 3.3. The spark was produced by external triggering a Continuum Surelite SLIII-10 Nd: YAG laser (up to 850 mJ, 1064nm pulse at 10 Hz). The laser light was focused using a biconcave lens (-50mm focal length) followed by a plano convex (200mm focal length) and finally focused to a spark by another plano convex lens (750mm focal length). A target (white card) was placed at the nozzle exit to ensure repeatable sparks could be obtain in order to minimize risk of damaging optics on the burner and duct.

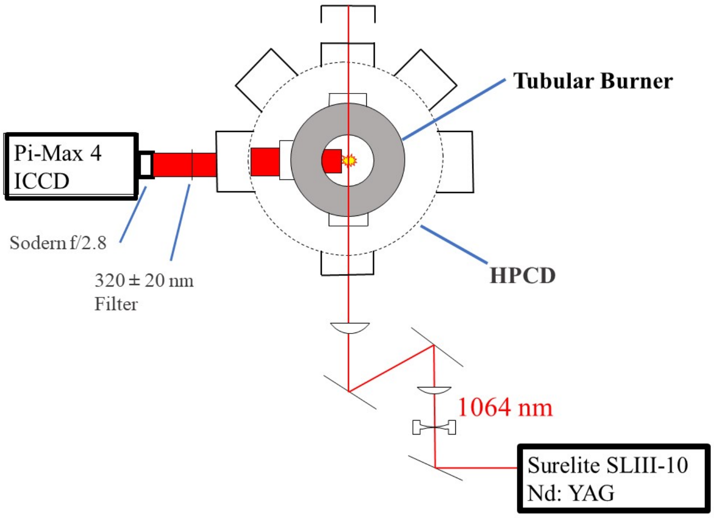

Figure 3.3: Schematic of laser spark system for the High-Pressure Combustion Duct (HPCD).

3.4 Chemiluminescence Imaging

Chemiluminescence imaging is a widely employed non-intrusive technique in a variety of combustion applications due to its natural occurrence within the flame. It has been used for the identification of the reaction zone [30, 31], as a heat release marker [32–35], and calculation of equivalence ratio [36, 37]. In the UV and visible spectrum, chemiluminescence emissions of hydrocarbon flames come from chemically excited OH^*, CH^*, C_2^* (where * denotes an electronically excited state) that can act as a "tracer" for flame diagnostics [38]. The simplicity of the technique allows for laser diagnostic methods such as Laser Induced Fluorescence (LIF) and Raman scattering to be used simultaneously. Therefore, chemiluminescence is a valuable visualization tool for combustion studies and applications.

The luminous emission in flames originates from the breakdown of the reactant species from an excited energy state to a relaxed ground state. The instantaneous radiation emission occurs at a specific wavelength for each unique species as seen in Figure 3.4. The equivalence ratio of the methane-air flames determines the amount of radicals generated within the flame. The concentration amounts of these radicals are based on their formation pathways. Interestingly, the emission intensity of OH^* has been found to be proportional to the local concentration of CH and O_2 [39]. The general formation pathway for OH^* is,

$$CH + O_2 \leftrightarrow CO + OH^* \tag{3.1}$$

Another possible formation pathway is

$$H + O + M \leftrightarrow OH^* + M \tag{3.2}$$

Regardless of the path, the emission of light is from the relaxation

$$OH^* \rightarrow OH + h_p \nu_f (light) \tag{3.3}$$

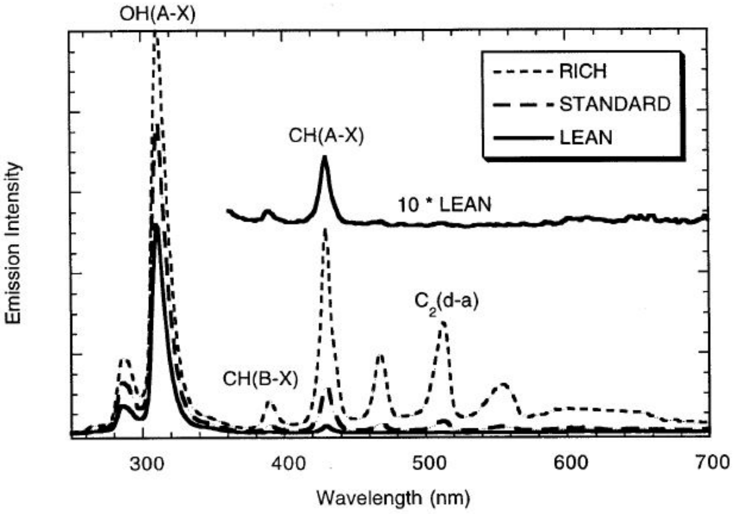

Fig. 1. Flame emission spectra from the center of the three low pressure premixed methane-air flames. The labeled insert is a 10-fold expansion of the lean flame spectrum.

Figure 3.4: Spectra of low pressure premixed methane-air flames. In this experimental campaign, a filter was used to capture OH^* at 320 nm with a FWHM of 40 nm. (Reprinted from Smith et al. [41], with permission from Elsevier).

where h_p is Planck's constant ($6.626 \cdot 10^{-34}\ \frac{m^2 kg}{s}$) and ν_f is the light's frequency. At low pressures, Equation 3.1 is the dominate pathway for OH^* formation due to CH being abundant in the reaction zone [40]. At higher pressures, Equation 3.2 becomes more important due to its third-body pressure dependence.

The excited molecules have a certain lifetime in the upper state after which they relax to ground state by spontaneous emission. Using appropriate filters and an ICCD camera, signal of the spontaneous emission of excited OH radicals will allow flame shape to be recorded. A schematic of the chemiluminescence imaging setup for High-Pressure Combustion Duct (HPCD) is shown in Figure 3.5. The flames were imaged using an ICCD camera (PI-MAX 4, 512x512 pixels) coupled to a UV lens (Sodern UV, f/2.8, 100mm) placed to look through one of the radially located flanges on the HPCD. The ICCD camera was set to an internal trigger frequency setting of 500 Hz with a 1000-ns gate delay. A bandpass filter (LaVision Advance at 320nm, FWHM 40nm) was used to observe OH chemiluminescence within the range of 280-310 nm [41]. To capture an axial image of the emissions, the camera was situated horizontally to a UV enhanced aluminum mirror (Edumund Optics) angled 45 degrees to the flame exhaust. During spark procedure, the shutter was fully closed to avoid saturating the camera. The burner is moved up and down on the vertical translation stage for ignition or signal collection as appropriate. Though the experimental setup is simple, this technique is only qualitative.

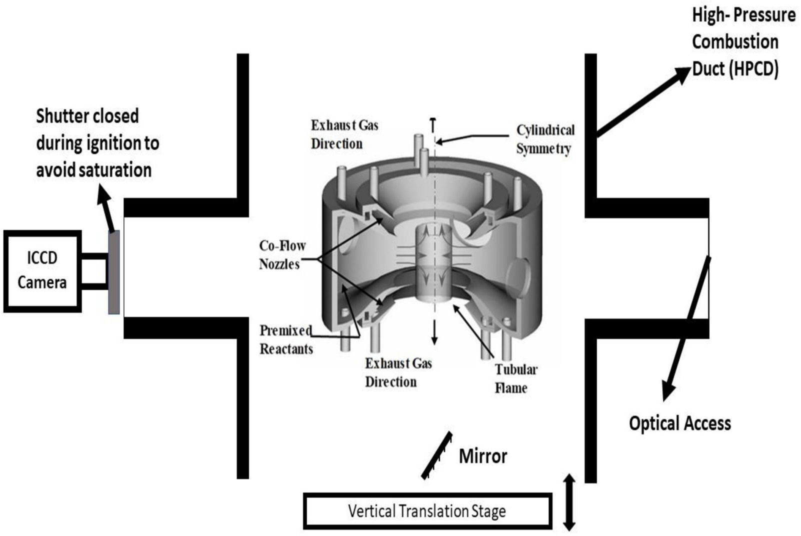

(a) During Spark Ignition

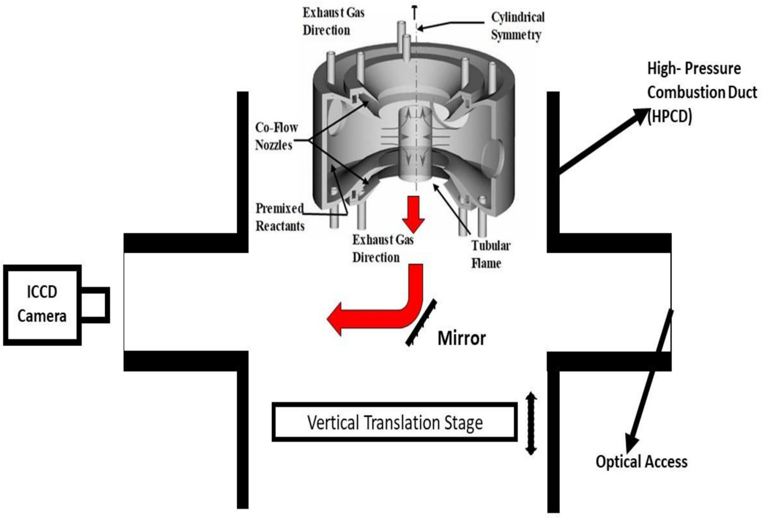

(b) During Data Collection

Figure 3.5: Chemiluminescence imaging setup for High-Pressure Combustion Duct (HPCD).

3.5 Flame Conditions

The experiments employed premixed flames at k = $200 s^{-1}$ to observe nearly equidiffusive Le flames by varying equivalence ratio (Φ). Inside the HPCD, methane and air are mixed at least 3 meters before entering the tubular burner to ensure adequate mixing. Flow rates are set with by fully automated mass flow controllers (Brooks SLA series), whose nominal accuracy is 1 percent of full scale.

All experimental conditions are listed in Table 3.1. For measurements, the equivalence ratio for the gases were adjusted by 0.02 increments to monitor changes the flame structures. The recorded flames are repeated at least three times to capture 600 images at each equivalence ratio. Turbulence occurs when the tubular burner's Reynolds number is above 2100, typically defined as:

$$Re = \frac{V D_h}{\nu} \tag{3.4}$$

Where, V is the velocity of the gas mixture at the nozzle exit, D_h is the hydraulic diameter (8 mm in this case), and ν is kinematic viscosity. It can be inferred from the table that the Reynolds number for higher stretch rates would be too great to produce a stable premixed flame [42].

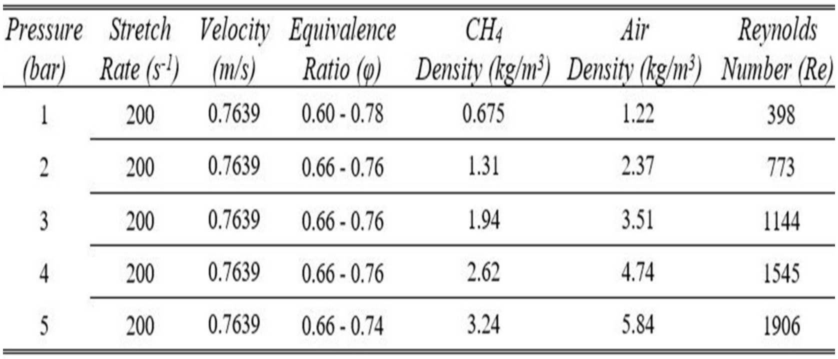

Pressure (bar)	Stretch Rate (s^{-1})	Velocity (m/s)	Equivalence Ratio (φ)	CH_4 Density (kg/m^3)	Air Density (kg/m^3)	Reynolds Number (Re)
1	200	0.7639	0.60 - 0.78	0.675	1.22	398
2	200	0.7639	0.66 - 0.76	1.31	2.37	773
3	200	0.7639	0.66 - 0.76	1.94	3.51	1144
4	200	0.7639	0.66 - 0.76	2.62	4.74	1545
5	200	0.7639	0.66 - 0.74	3.24	5.84	1906

Table 3.1: List of experimental conditions for high-pressure methane-air tubular flames.

3.6 Direct Numerical Simulation

3.6.1 In-House Code

Numerical simulation offers the opportunity to supplement theory and experiment. It is imperative to simultaneously solve the conservation of mass, species, momentum, and energy equations to develop accurate models for combustion. Computational models utilizing these equations in three dimensions are complex, especially if attempting to capture all phenomena over small spatial and temporal scales. An in-house code [7] has been developed to solve the conservation equations for the tubular burner in the radial and tangential domains which are functions of r and θ. The data presented in this work utilizes the same code, but the theta domain is reduced to small value, thus providing a one-dimensional solution. For 2D campaigns, an angular section ($r \epsilon \ [0, R]$, $\theta \epsilon \ [0, \ 2\pi/N_c]$) can be selected to force N_c flame-cell symmetry, ($[\ 2\pi/N_c]$).

The axial direction (z) is expressed as a product of the axial coordinate and axial velocity gradient, W, due to strong strong unidirectional flow divergence [43]. The velocity field, $\boldsymbol{u}$, is expressed as:

$$\boldsymbol{u} = u_r(r,\theta)\hat{r} + u_\theta(r,\theta)\hat{\theta} + u_z W(r,\theta)\hat{z} \tag{3.5}$$

where $\hat{r}, \hat{\theta}, \hat{z}$ are unit vectors; u_r, u_θ, u_z are the radial, tangential, and axial velocity components. In addition, the axial dependence on the perturbed pressure field, $\tilde{p}_1$, can be equated to the scalar pressure value, H, defined as:

$$H = \frac{1}{z}\frac{\partial \tilde{p}_1}{\partial z} \tag{3.6}$$

The above equation is integrated allowing $\tilde{p}_1$ to be implemented as:

$$\tilde{p}_1 = \frac{z^2}{2}H + I(r,\theta) \tag{3.7}$$

where I is the radial and tangential pressure dependence.

3.6.2 Governing Equations

The model consists of n+6 primitive variables (u_r, $\frac{u_\theta}{r}$, Y_i [Mass fraction], W, H, I, T [Temperature]) described in Nomenclature and formulated as follows:

Mass Conservation:

$$0 = \frac{\partial}{\partial r}\left(r\rho u_r\right) + \frac{\partial}{\partial \theta}\left(\rho u_\theta\right) + r\rho W \tag{3.8}$$

where ρ is the density.

Radial momentum conservation:

$$\begin{split} 0 = \rho\left(u_r\frac{\partial u_r}{\partial r} + \frac{u_\theta}{r}\frac{\partial u_r}{\partial \theta} - \frac{\nu^2}{r}\right) + \frac{\partial I}{\partial r} - \frac{1}{r}\frac{\partial}{\partial r}\left(2\mu r\frac{\partial u_r}{\partial r}\right) - \\ \frac{1}{r}\frac{\partial}{\partial \theta}\left[\mu\left(r\frac{\partial}{\partial r}\left(\frac{u_\theta}{r}\right) + \frac{1}{r}\frac{\partial u_r}{\partial \theta}\right)\right] - \mu\frac{\partial W}{\partial r} + \frac{2\mu}{r}\left(\frac{1}{r}\frac{\partial u_\theta}{\partial \theta} + \frac{u_r}{r}\right) \end{split} \tag{3.9}$$

where μ is the mixture viscosity.

Azimuthal momentum conservation:

$$\begin{split} 0 = \rho\left(u\frac{\partial u_\theta}{\partial r} + \frac{u_\theta}{r}\frac{\partial u_\theta}{\partial \theta} - \frac{u_r u_\theta}{r}\right) + \frac{1}{r}\frac{\partial I}{\partial \theta} - \frac{1}{r^2}\frac{\partial}{\partial r}\left(\mu r^2\left(r\frac{\partial}{\partial r}\left(\frac{u_\theta}{r}\right) + \frac{1}{r}\frac{\partial u_r}{\partial \theta}\right)\right) - \\ \frac{1}{r}\frac{\partial}{\partial \theta}\left[2\mu\left(\frac{1}{r}\frac{\partial u_\theta}{\partial \theta} + \frac{u_r}{r}\right)\right] - \frac{\mu}{r}\frac{\partial W}{\partial \theta} \end{split} \tag{3.10}$$

Axial momentum conservation:

$$0 = \rho\left(u_r\frac{\partial W}{\partial r} + \frac{u_\theta}{r}\frac{\partial W}{\partial \theta} + W^2\right) + H - \frac{1}{r}\frac{\partial}{\partial r}\left(\mu r\frac{\partial W}{\partial r}\right) - \frac{1}{r}\frac{\partial}{\partial \theta}\left(\frac{\mu}{r}\frac{\partial W}{\partial \theta}\right) \tag{3.11}$$

Energy conservation:

$$0 = \rho \left(u_r \frac{\partial T}{\partial r} + \frac{u_\theta}{\theta} \right) + \frac{1}{r c_p} \frac{\partial}{\partial r} \left(r q_r - r \sum_{i \epsilon S} h_i \rho Y_i u_{r_i^d} \right) + \frac{1}{r c_p} \frac{\partial}{\partial \theta} \left(r q_\theta - r \sum_{i \epsilon S} h_i \rho Y_i u_{\theta_i^d} \right) + \frac{1}{c_p} \sum_{i \epsilon S} \left(\rho Y_i u_{r_i^d} c_{p_i} \frac{\partial T}{\partial r} + \rho Y_i u_{\theta_i^d} c_{p_i} \frac{1}{r} \frac{\partial T}{\partial \theta} \right) + \frac{1}{c_p} \sum_{i \epsilon S} (\omega_{si} h_i m_i) + \frac{Q_{rad}}{c_p} \tag{3.12}$$

where c$_p$ is the mixture heat capacity, q is the heat flux in the radial (subscript r) or tangential (subscript θ) direction, h is the mixture enthalpy, ω_s is the species production rate, m is the molar mass of a species, Q_{rad} is the radiative heat loss, S represents the range of present species, i represents the subscripts in a given species in S, and the superscript d on the velocity terms refers to diffusive velocities.

Species conservation:

$$0 = \rho \left(u_r \frac{Y_i}{r} + \frac{u_\theta}{r} \frac{\partial Y_i}{\partial \theta} \right) + \frac{1}{r} \frac{\partial}{\partial r} \left(r \rho u_{r_i^d} Y_i \right) + \frac{1}{r} \frac{\partial}{\partial \theta} \left(\rho u_{\theta_i^d} Y_i \right) - \omega_{s_i} m_i, \quad i \epsilon S \tag{3.13}$$

To enforce a uniform value for H without the velocity boundary conditions over-specifying the problem, the following is added:

$$0 = \frac{\partial H}{\partial r} \tag{3.14}$$

with the boundary condition:

$$0 = \frac{\partial H}{\partial \theta} \tag{3.15}$$

Radiation heat loss, Q_{rad}, is assumed to occur in optically-thin form for heated water, carbon monoxide, and carbon dioxide as:

$$Q_{rad} = 4\sigma \left(T^4 - T_b^4 \right) p_o \sum_i \left(X_i a_i \right), \quad i \epsilon \{H_2O, CO_2, CO\} \tag{3.16}$$

where σ is the Stefan-Boltzmann constant($5.67 \cdot 10^{-8} \ \frac{W}{m^2 K^4}$), T_b is the background temperature, and a_i is the Planck mean absorption coefficient of species i (in [44]).

The scalar thermodynamic pressure, p_o, is used with the ideal gas constitutive equation:

$$p_o = \rho RT \sum_{i\epsilon S} \frac{Y_i}{m_i} \tag{3.17}$$

While the flow acceleration is low enough to neglect pressure diffusion, mass and thermal diffusions must be considered and are expressed in vector form:

$$\rho Y_i \boldsymbol{u}_i^d = -\sum_{j\epsilon S} Y_i D_{ij} \nabla X_j - Y_i D_i^T \nabla lnT, \quad i\epsilon S \tag{3.18a}$$

$$\boldsymbol{q} = \sum_{i\epsilon S} h_i \rho Y_i \boldsymbol{u}_i^d - \lambda \nabla T + \boldsymbol{q}^D \tag{3.18b}$$

where X is mole fraction, λ is heat conductivity, and $\boldsymbol{q}$ is heat flux field. Mass diffusion coefficients, D_{ij}, and thermal diffusion terms, $Y_i D_i^T$ ∇lnT and $\boldsymbol{q}^D$ from Soret and Dufour effects. The Soret effect is characterized as mass flux a result of temperature gradients, and the Dufour effect is heat flux from concentration gradients. These effects are calculated from EGLIB [45] and expressed in terms of computational variables $\tilde{D}_{ij}$ and $\tilde{X}_i$:

$$Y_i D_{ij} = \rho \tilde{D}_{ij}, \quad j\epsilon S \tag{3.19a}$$

$$Y_i D_i^T = \rho \sum_{j\epsilon S} \tilde{D}_{ij} \tilde{X}_j X_j, \quad j\epsilon S \tag{3.19b}$$

$$\boldsymbol{q}^D = p_o \sum_{i\epsilon S} \frac{m}{m_i} \tilde{X}_i Y_i \boldsymbol{u}_i^d \tag{3.19c}$$

where the m term refers to mean molar mass when not modified by a subscript. An adaptive finite difference method with pseudo-transient continuation [46] and Newton search have been employed. A further detailed discussion can be found in [7] and are not repeated here. Previous atmospheric tubular flame endeavours have shown good overall agreement between the experiments and simulations utilizing this in-house code [7, 17, 47].

3.6.3 Boundary Conditions

All variables have azimuthal symmetry except for v which is set to 0 at $\theta = 0$ to prevent arbitrary rotation of the flame to arrive at the time-steady solution.

Radial boundary conditions at the outer nozzle (r=R) are specified by:

$$u_r = u_{rBC} \quad \frac{u_\theta}{r} = 0 \quad W = W_{BC}$$
$$Y_i \left(u_r + u_{r\,i}^{\,d} \right) = \left(Y_i u_r \right)_{BC} \quad T = T_{BC}$$

with the following exit (r = 0) conditions at the centerline:

$$u_r = 0 \quad \frac{u_\theta}{r} = 0 \quad \frac{\partial W}{\partial r} = 0 \quad \frac{\partial Y_i}{\partial r} = 0 \quad \frac{\partial T}{\partial r} = 0 \quad I = 0$$

3.6.4 Kinetics and Transport

Detailed chemical kinetics and transport properties are used with the governing equations to describe the interaction of species with combustion phenomena. The methane-air thermochemical and transport mechanisms along with their databases used in this study are GRI-Mech 3.0 [48] and San-Diego [49]. The chemical kinetic mechanisms use 325 and 272 reversible reactions which comprise 53 and 50 species, respectively. The species mole fractions from these mechanisms are also compared and evaluated to chemical equilibrium. Zero-dimensional chemical equilibrium calculations were performed using the software GASEQ. The fundamentals of the program are based on thermodynamic and transport properties defined by NASA CEA [50]. These numerical calculations analyzing high-pressure flames are critical to determining their accuracy to experimental measurements.

Chapter VI

RESULTS & DISCUSSION

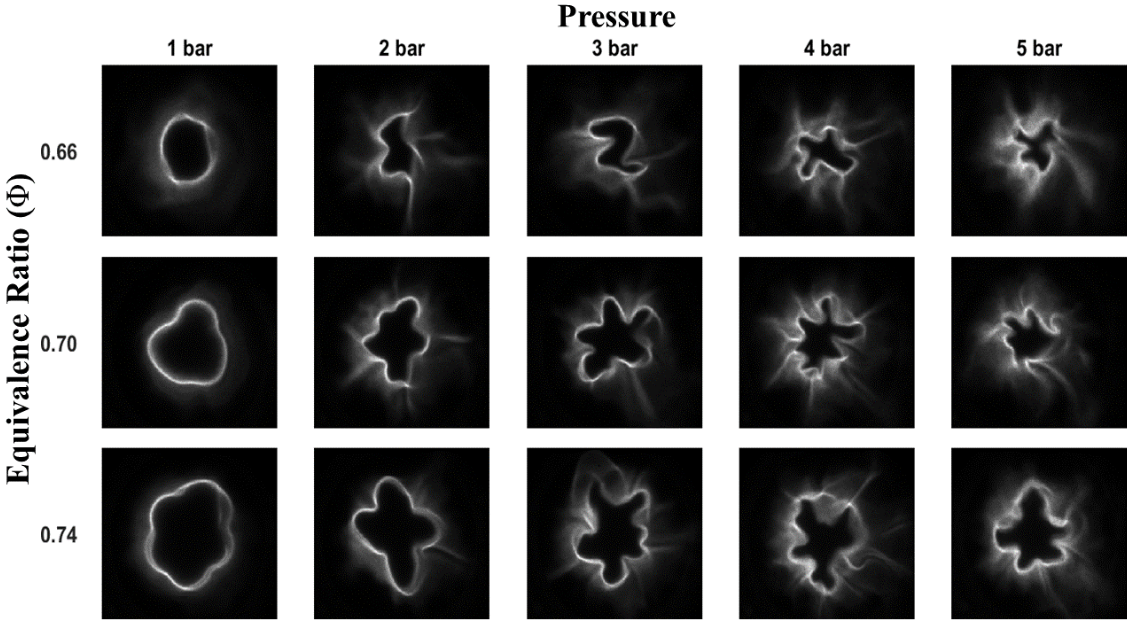

Figure 4.1: Raw instantaneous images of high-pressure methane-air flames ($k = 200 s^{-1}$) by variance in equivalence ratio. Each image has a field of view approximately 30 mm square and is imaged at the exit of the Tubular Burner. The white outer wisps at higher pressures are exhaust fumes captured during the imaging process.

The first experimental images of lean methane-air flames at high-pressure can be seen in Figure 4.1. Since the recorded cases above 1 bar are limited, equivalence ratios 0.66, 0.70, and 0.74 are considered for the following analysis. At atmospheric pressure, lean methane-air flames show instabilities in the form of wrinkling with increasing equivalence ratio. This behavior is expected as equidiffusive ($Le \approx 1$) methane-air flames have been shown to wrinkle rather than form cells through the absence of strong thermal-diffusive effects. At higher pressures, the wrinkling effect is no longer strongly correlated to the equivalence ratio. Premixed tubular flames are convex (positively curved) to the incoming reactant flow, and on top of the Le effects, the flame wrinkles experience an enhancement of mass diffusivity from stretch and curvature. The positive curvature also enhances local stoichiometry and flame speed which allows the flames to stabilize even at high pressures [14].

The unsteady nature of these flames is likely a combination of cross flow from the HPCD and PIV particles somewhat obstructing the inlet flow of the tubular burner. Under elevated conditions, the coupling of the times scales for the flow field, molecular transport, and chemical kinetics leads to unsteady flame characteristics [51]. This and the presence of the PIV particles creates tubular flame shapes like in Figure 4.2. At atmospheric conditions, the wrinkles show some dependence on equivalence ratio with some level of symmetry. At high pressure, the tubular flames starts to exhibit a non-axisymmetric shape even at the same condition ($\phi = 0.7$ and $k = 200s^{-1}$). The wrinkles of these methane-air flames are a real result of slightly sub-unity Lewis number. Previous investigations have shown that at atmospheric conditions tubular methane-air flames will wrinkle [14]. It is difficult at this time to be certain whether the unsteadiness is a result of the crossflow of the HPCD or PIV particles.

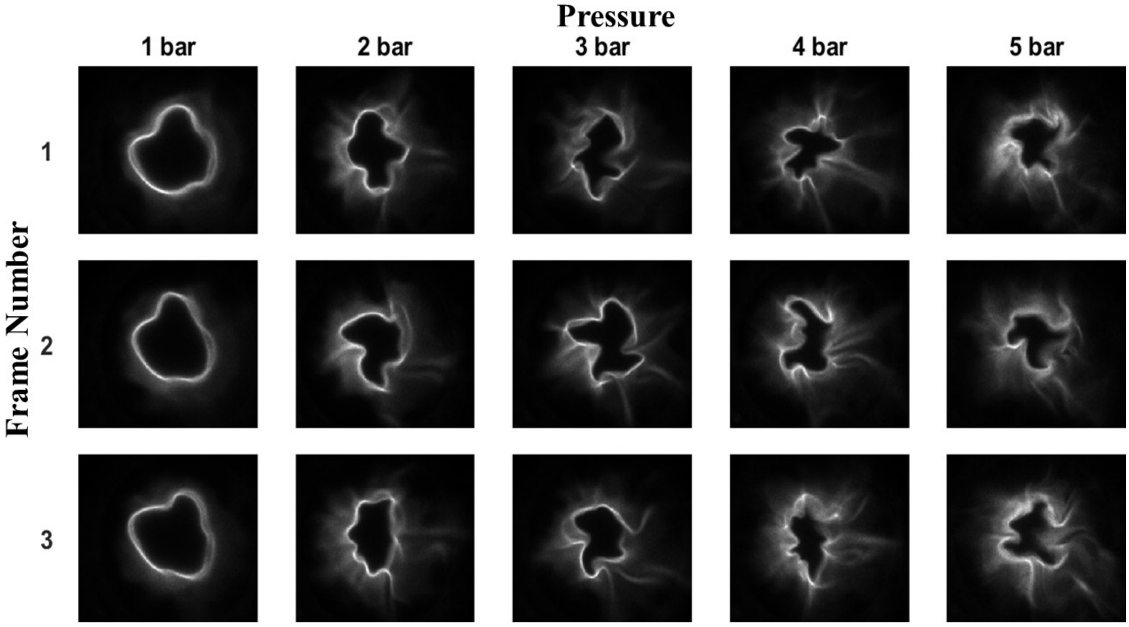

Figure 4.2: Raw instantaneous images of high-pressure methane-air flames at $\phi = 0.7$ and $k = 200s^{-1}$. Rows 2 and 3 represent the next immediate frames to illustrate how quickly the flame shape varies. The combination of crossflow from the HPCD and titanium oxide particles that generate unstable flame patterns. Each image has a field of view approximately 30 mm and is imaged at the exit of the Tubular Burner.

4.1 Flame Structure/Features

In previous studies [18, 20], the overall tubular flame radius, thickness, and speed was predicted to decrease with increasing pressure. Direct numerical simulations and experiments show a similar trend in Figures 4.3, 4.6 and 4.8. At k = 200s^{-1} and ϕ = 0.7, discrepancies exist between experimental and numerical data on the flame radius. The simulations predict a much smaller flame radius especially at pressures of 5 bar as seen in Figure 4.3. The large discrepancies between data and simulations are likely a result of unsteady effects, an incorrect nonzero stretch boundary condition (W) (See Appendix A.1), and limiting the simulations to 1D rather than 2D. The k = 400s^{-1} data is expected to have a decreasing radii as stretch is inversely proportional. The interesting note is that the radii for k = 400s^{-1} is half of k = 200s^{-1} at higher pressures. This data provides insight that even at different stretch rates there is a decreasing trend in flame radius with pressure.

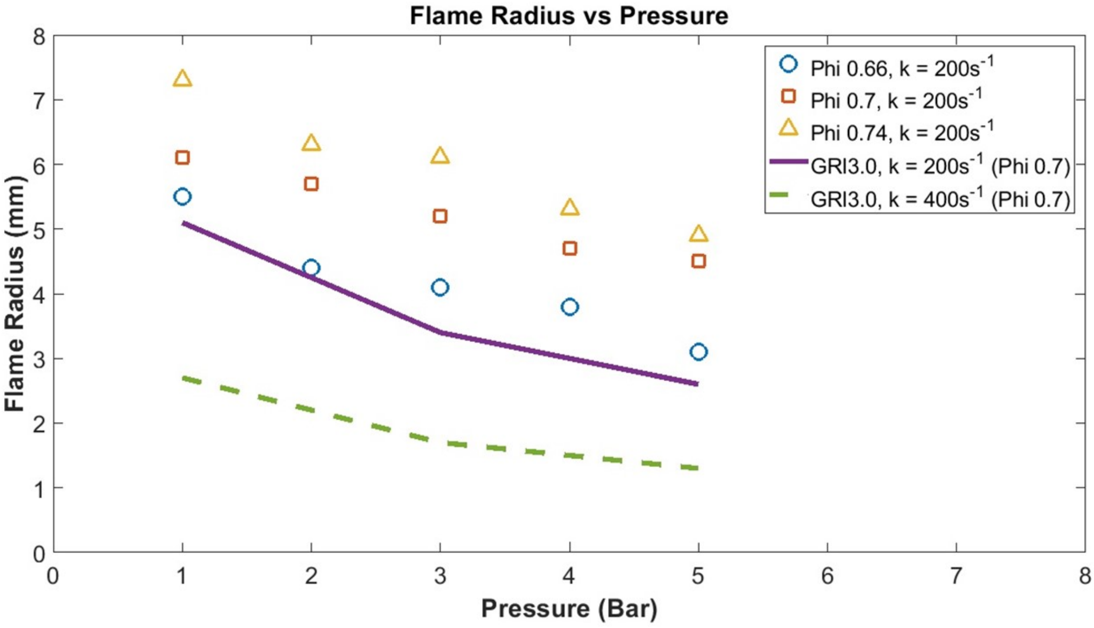

Figure 4.3: Experimental(points) and numerical(lines) radii as a function of pressure. All experimental points are from a stretch of k = $200s^{-1}$. The non-zero stretch boundary for all k = $200s^{-1}$ numerical cases is 50. The non-zero stretch boundary for k = $400s^{-1}$ numerical cases is 120. At $\phi = 0.7$, the $200s^{-1}$ numerical simulations underpredict the flame radii of experimental data up to nearly 55% at 5 bar.

The experimental radii were determined by calculating the mean of the outer (r_o) and inner (r_i) radius of the tubular flame. Figure 4.4 is an example of averaged (600 images) methane-air flames pre- and post-binarization at 1 bar, k = 200s^{-1}, and $\phi = 0.7$. The distance formula was used to calculate the distance between the center (blue dot) and boundaries (blue rings). As mentioned earlier, the presence of titanium oxide particles from the HPCD made it difficult to determine more flame features such as thickness for this study.

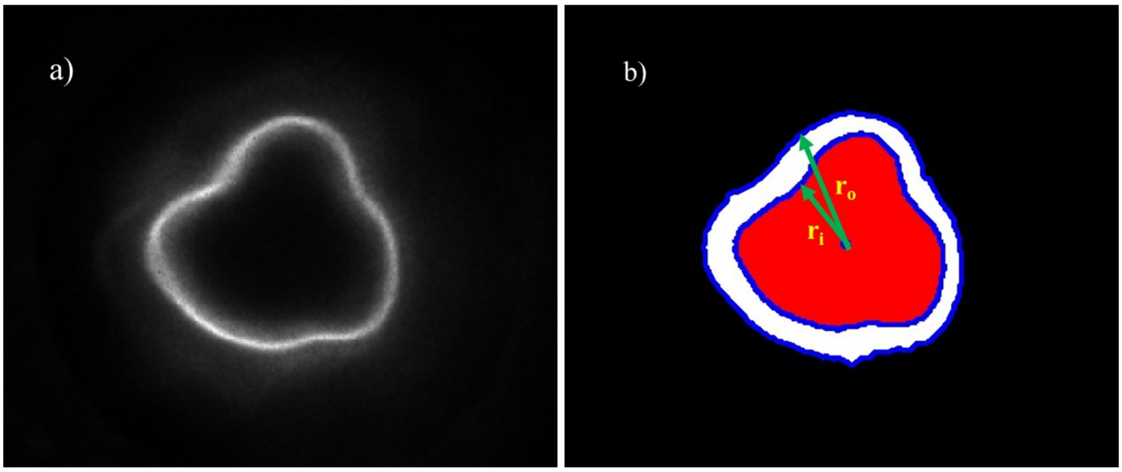

Figure 4.4: Averaged images from methane-air flames at 1 bar, k = 200s^{-1}, and ϕ = 0.7. Images a) and b) are the pre- and post-binarization. The variables r_o and r_i represent the outer and inner radius of the tubular flame.

In Figure 4.6, thicknesses of tubular and burner-stabilized flames show a similar decreasing trend even at different equivalence ratios. The simulations from Glassman [19] utilize a freely propagating, one-dimensional, adiabatic flame based on the scheme of [52]. Also, Glassman calculates flame thickness as the difference between the point at which one of the reactant mole fractions begins to decay and the initial point at which heat release begins to taper off sharply. The tubular burner simulations were calculated by thickness of slope of the temperature profiles as shown in Figure 4.5.

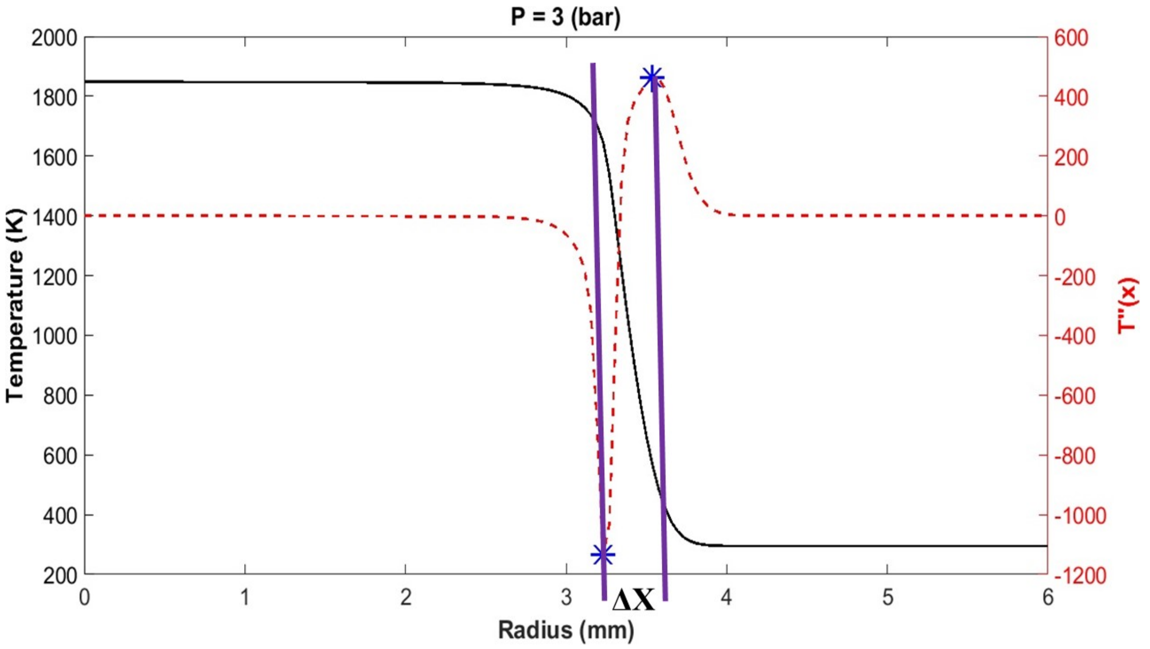

Figure 4.5: An example flame profile at P = 3 bar, $\phi = 0.7$, and k = $200s^{-1}$ showing how the tubular burner thicknesses were calculated. The concavities of the second derivative of the temperature give an estimation of the points where the slope begins to change.

Mathematically, flame thickness can be calculated by,

$$\delta_L = \frac{\alpha}{S_L} \tag{4.1}$$

where δ_L is flame thickness, α is thermal diffusivity, and S_L is flame speed. The diffusion of heat and mass into flame is based on the reaction rate and that determines the size of the flame zone and temperature gradient. As pressure increases, the diffusion rates decrease and thus the flame zone begins to thin.

The downward trend in both thickness and radius can be directly attributed to the decreasing flame speeds. The flame speed is defined as the velocity at which the unburned gases move through the combustion wave. Graphically, the flame velocities for all cases were determined at the first instance of a temperature rise in the flame simulations. This is the instance where the flame propagation is balanced by the momentum of the reactant mixture.

The correlation between flame speed to thermal diffusivity and pressure is given

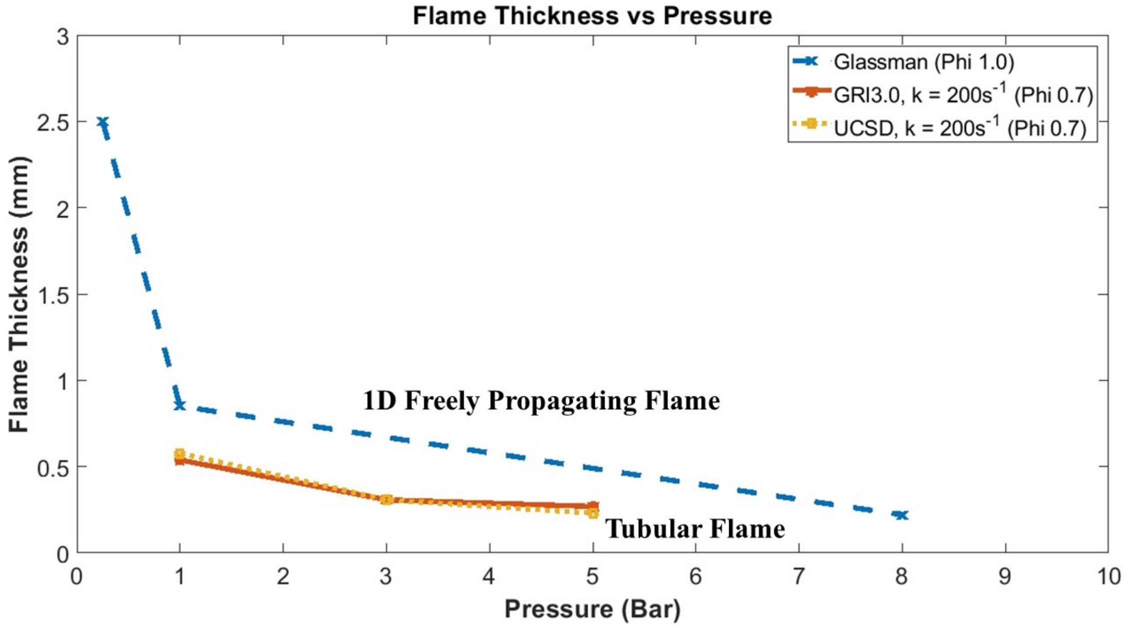

Figure 4.6: All simulation profiles of flame thickness as a function of pressure. Glassman is a 1D freely propagating planar flame simulation while all other simulations are a tubular flame. Glassman is based on different numerical scheme and equivalence ratio using pressures of 0.25, 1, and 8 bar. Even with a difference in flame simulations, they show good agreement in trends at high pressure.

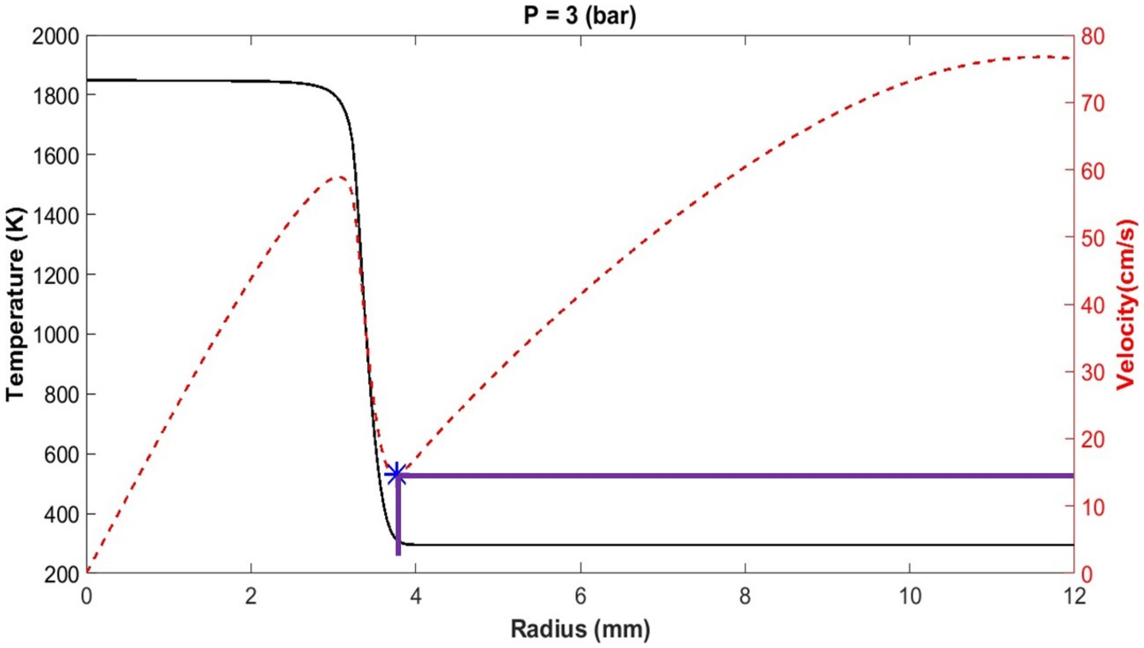

Figure 4.7: An example flame profile at P = 3 bar, $\phi = 0.7$, and k = $200s^{-1}$ showing how the tubular burner velocities were calculated. The flame speed (S_L) corresponds to velocity at the first perceptible rise in temperature.

by the expressions:

$$S_L \approx \sqrt{\alpha RR} \tag{4.2a}$$

$$S_L \approx \sqrt{P^{n-2}} \tag{4.2b}$$

where RR is the reaction rate and n is the overall reaction rate. The pressure dependence on flame speed can be best explained by the second and third-order reactions:

$$H + O_2 \rightarrow O + OH \tag{4.3}$$

$$H + O_2 + M \rightarrow HO_2 + M \tag{4.4}$$

Equation 4.4 directly competes with similar and lesser pressure dependent (Equation 4.3) processes for H atoms in the flame. The competition between reactions at high pressures will begin to impede combustion, and that becomes apparent through the reduction of flame temperature and speed. There have been a variety of burner configurations that show the same downward trend in flame speed for stoichiometric($\phi = 1.0$) methane-air flames at high pressure [53, 54]. In Figure 4.8, the flame speeds of tubular and burner-stabilized flames show a similar decreasing trend even at different equivalence ratios. The higher flame speeds of Glassman are a result of more fuel concentration into the 1D freely propagating flame. The tubular flame results at k = 200s^{-1} with and without radiation have differences less than 1%. The 400s^{-1} data has a higher flame speed than 200s^{-1}, and that increase demonstrates preferential diffusion. As seen later, the flame temperature is higher at the higher stretch of 400s^{-1}. The flame speeds for k = 400s^{-1} at 1, 3, 5 bar is 9%, 12%, 13%, respectively, higher than the 200s^{-1} data. Although not experimentally determined in this study, based on measured radii, experimental flame speed and thickness would show the same decreasing trend due to the H atom effect.

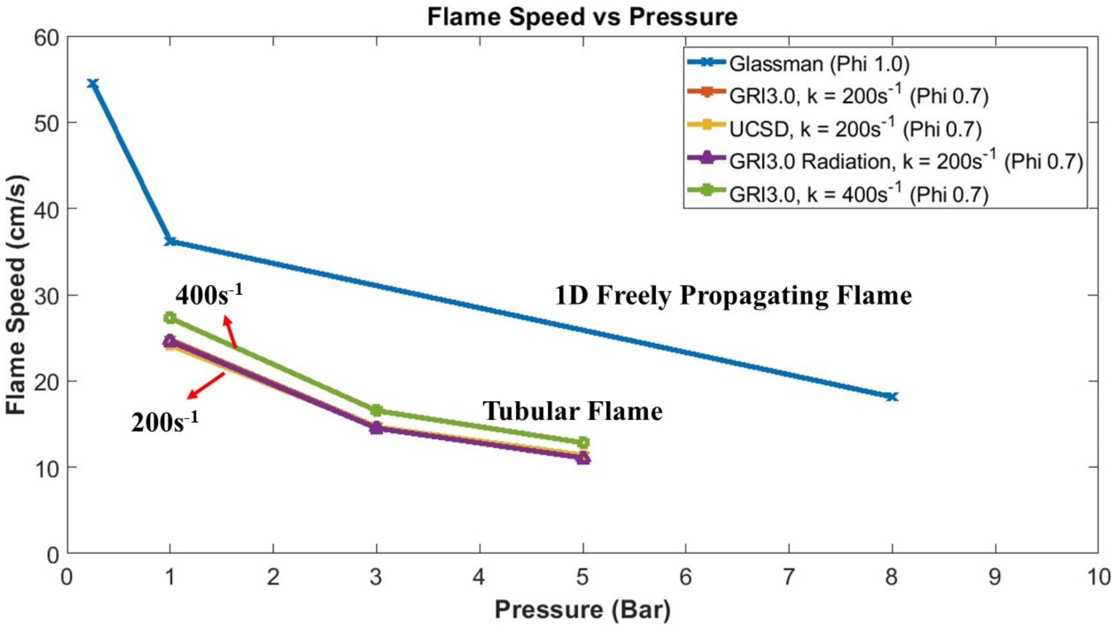

Figure 4.8: All simulation profiles of flame speed as a function of pressure. Glassman is a 1D freely propagating planar flame simulation while all other simulations are a tubular flame. Even with a difference in flame simulations, they show good agreement in trends with pressure. Note: There are overlapping lines with the GRI3.0 (with and without radiation) and UCSD because they are at k = $200s^{-1}$.

4.2 Numerical Comparisons

4.2.1 Mechanism Comparison

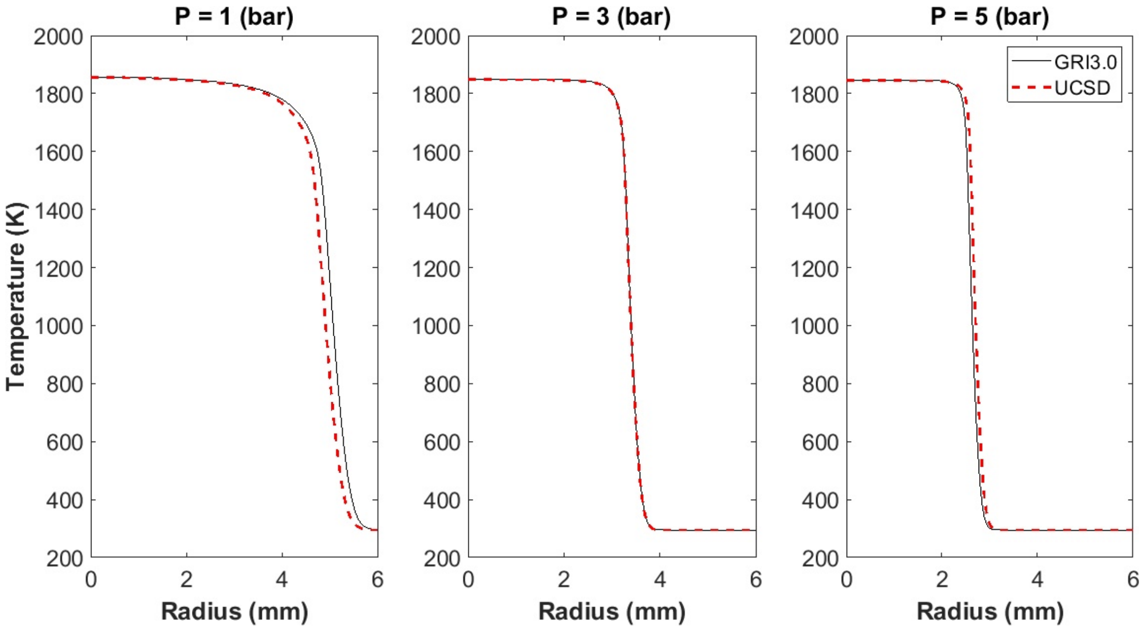

Figure 4.9: Simulation temperature profiles for three representative pressures of GRI3.0 and UCSD at k = $200s^{-1}$.

Figures 4.9-4.13 show the comparison of the flame temperature and species distribution of both UCSD and GRI3.0 mechanisms at 1, 3, and 5 bar for the same stretch rate of $200s^{-1}$. The difference between peak species values for all conditions are less than 3%. At 1 bar, GRI3.0 estimates a slightly larger flame radius that is a result of a higher flame speed (24.79 cm/s) than UCSD (24.15 cm/s). Good agreement of flame radii, temperature, and species composition for both mechanisms can be seen at 3 bar. At 5 bar, UCSD predicts a slightly larger flame radius even at a lower temperature (1K difference). This can be attributed to the flame speed at 5 bar for UCSD (11.41 cm/s) being slightly faster than GRI3.0 (11.22 cm/s). Even at an elevated pressure, UCSD predicts the tubular flame is able to propagate 0.2 mm further away from the centerline. This is likely due to the fewer number of reactions in the mechanism ($\approx$ 52 less) competing for H atoms compared to GRI3.0.

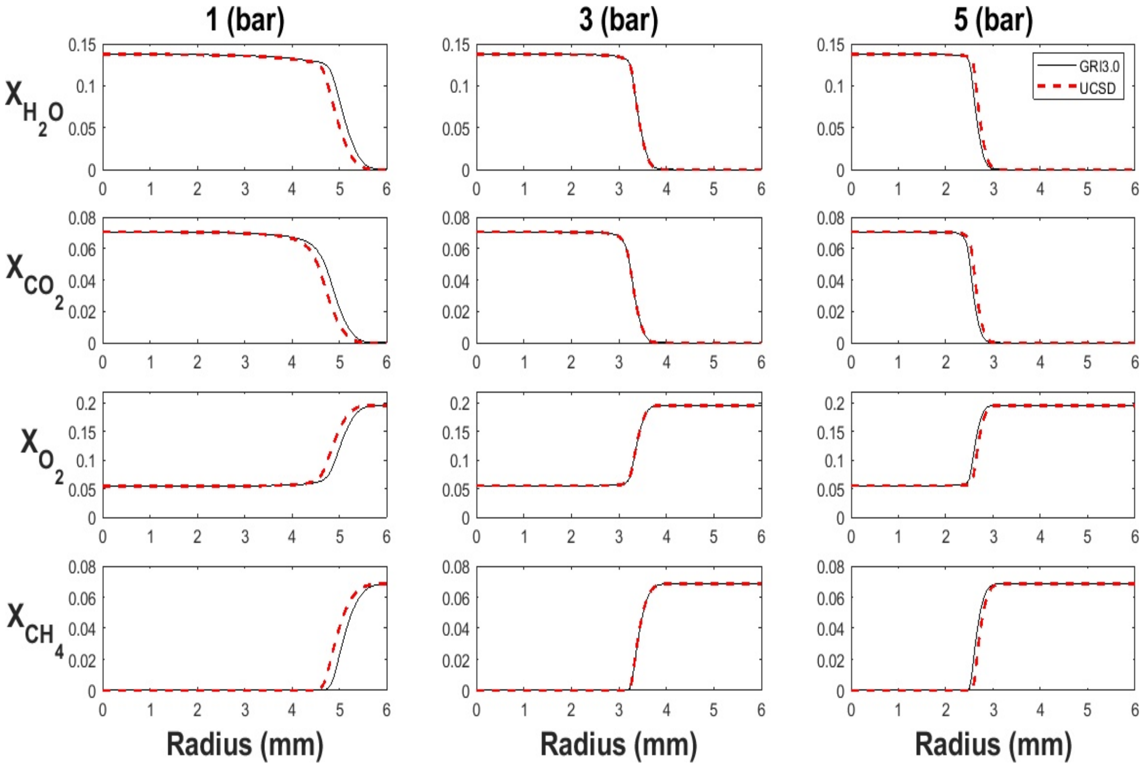

Figure 4.10: Mechanism comparison of flame structure for main species distributions with increasing pressure at k = $200s^{-1}$.

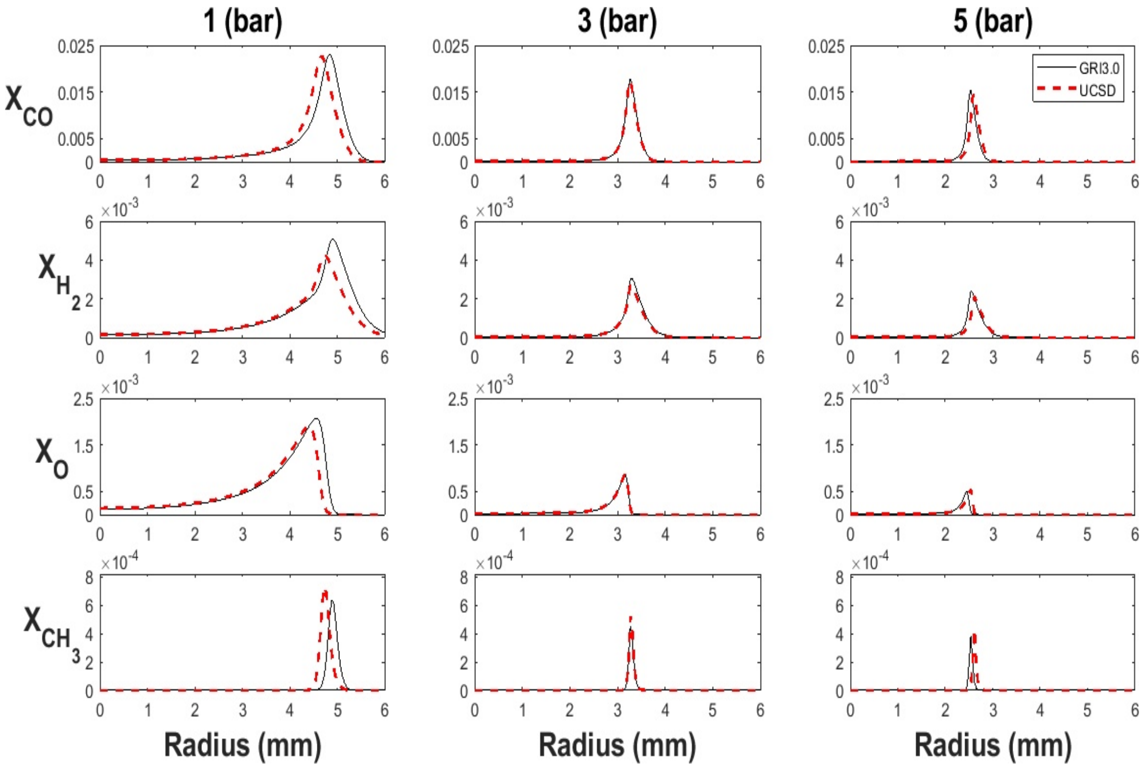

Figure 4.11: Mechanism comparison of flame structure for intermediate species and radicals distributions with increasing pressure at k = $200s^{-1}$.

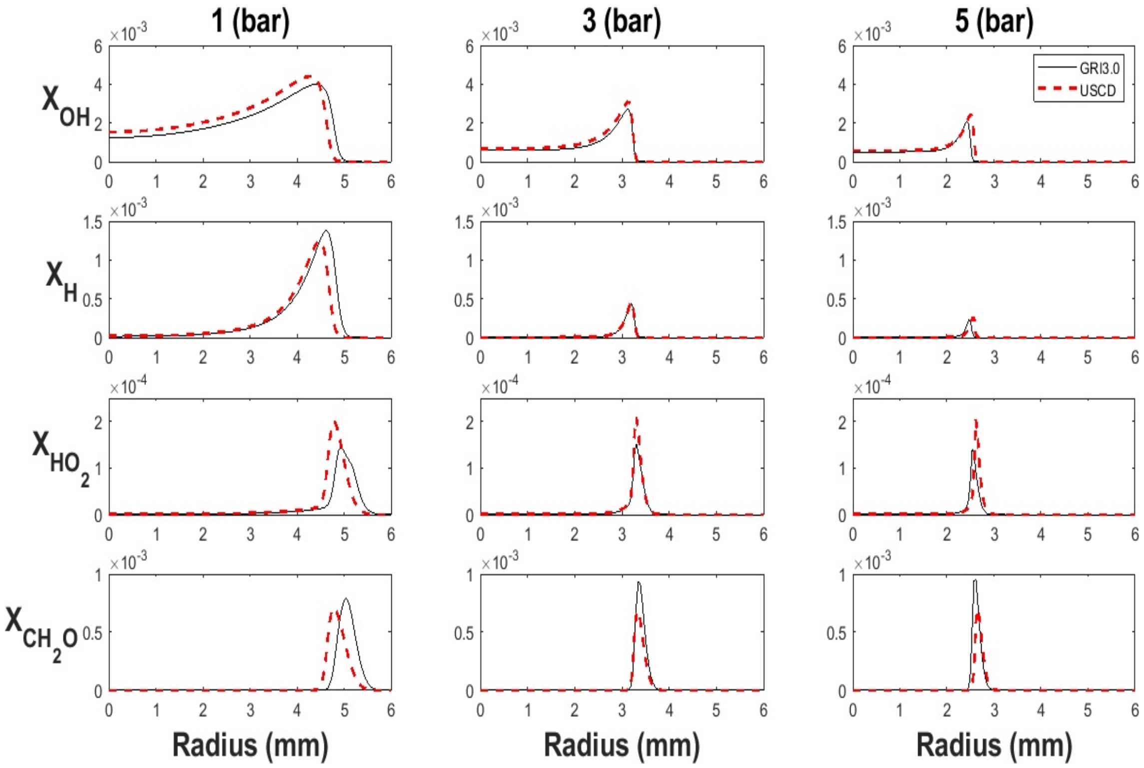

Figure 4.12: Mechanism comparison of flame structure for intermediate species and radicals distributions with increasing pressure at k = $200s^{-1}$.

4.2.2 Radiation Comparison (GRI3.0)

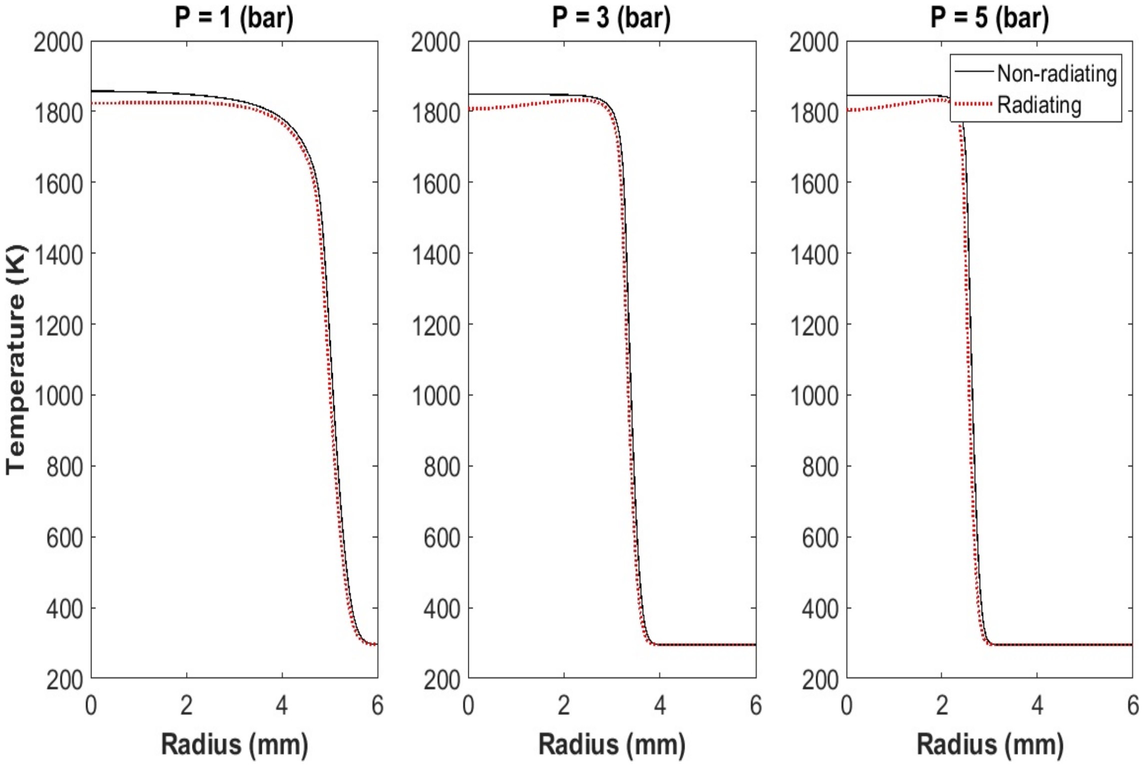

Figure 4.13: Simulation temperature profiles for three representative pressures of GRI3.0 with and without radiation at k = 200s^{-1}. The centerline differences between radiation and non-radiation are 33 K, 41 K, and 42 K at 1, 3, and 5 bar, respectively.

Radiation plays an critical role in heat transfer as well as all types of combustion systems. Figure 4.13 shows the comparison of the flame structure of GRI3.0 with and without radiation at 1, 3, and 5 bar for the same stretch rate of $200s^{-1}$. Further plots of main, radical, and intermediate species can be found in Appendix A.2. The radiating species are H_2O, CO_2, and CO based on being strong absorbers and emitters of radiant energy [55]. The overall shape of the temperature plots are not too different than from the previous comparison. The flame radius of the plots are expected as the radiation scheme has a flame speed of approximately 1% less than its counterpart.

The heat loss in 1, 3, and 5 bar as a result of the radiation leads to centerline temperature differences of 33 K, 41 K, and 42 K, respectively. Previous numerical simulations have shown that radiation heat loss decreases flame temperature at high stretch rates (k $> 4s^{-1}$) for lean ($\phi = 0.46$) premixed methane-air tubular flames by stretched-induced incompletion [11]. As stretch rate increase, the tubular flame temperature increases until the combination of radiation heat loss and short residence times cause extinction. In Figure 4.13, the addition of high pressure causes a slightly greater temperature drop of 41 k and 42 k at 3 and 5 bar, respectively. It appears the higher pressure causes even shorter residence times for completion, although the temperature loss from 3 and 5 bar is similar. One would suspect that tubular flames at higher stretch rates would have a larger temperature difference due to radiation and more incomplete reactions. However, preferential diffusion would mitigate the radiation heat loss within the tubular flame.

4.2.3 Stretch Rate Comparison (GRI3.0)

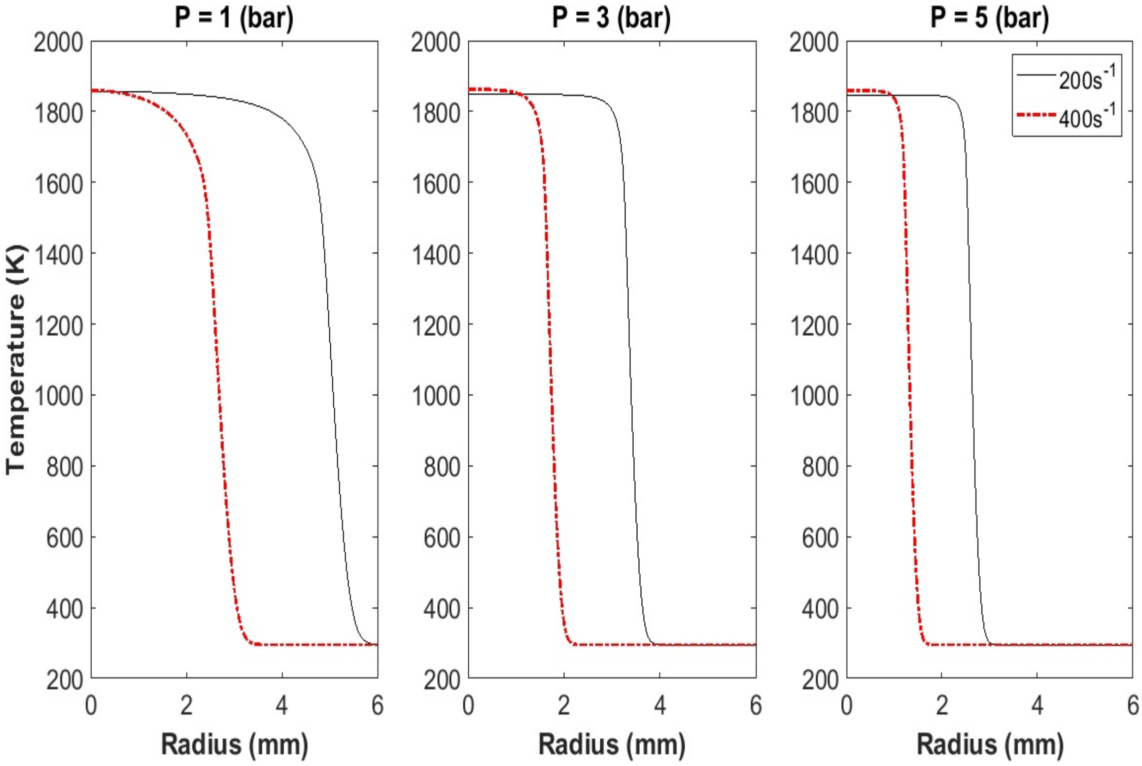

Figure 4.14: Simulation temperature profiles for three representative pressures of GRI3.0 at $200s^{-1}$ and $400s^{-1}$.The centerline differences between 200^{-1} and $400s^{-1}$ are 3 K, 15 K, and 14 K at 1, 3, and 5 bar, respectively.

The extent at which flame stretch rate influences combustion characteristics in the presence of a high pressure flow field has been of great interest in combustion science. Figure 4.14 shows the comparison of the flame structure of GRI3.0 at 1, 3, and 5 bar for $200s^{-1}$ and $400s^{-1}$. Further plots of main, radical, and intermediate species can be found in Appendix A.3. The $400s^{-1}$ cases naturally produce smaller diameter flames as a result of greater stretch in the axial coordinate. As previously predicted, tubular flame temperature and speed increases with increasing stretch rate and pressure. This increase in temperature and flame speed is a result of enhancement from preferential diffusion. The decrease in temperature at 5 bar could be due to the smaller flame radius. The flame temperature depends on the residence time of the reactants inside the flame to become consumed. At an extreme pressure (5 bar), reactants are likely being ejected out into the flow environment before being broken down within the flame (Damköhler number much less than one).

Zhang et al.[20] predicts a higher temperature for k = $200s^{-1}$ tubular flames at atmospheric pressure. In their analysis, they employed a modified OPPDIF software [56] with methane kinetics represented using GRI3.0. At k = $200s^{-1}$, they estimate the flame temperature to be 1865 K. In comparison to Figure 4.14, the temperature difference at 1 bar is about 8 K, which is small when compared to a flame temperature of 1857 K. When extrapolating their data further to k = $400s^{-1}$, it would appear that they would predict a lower temperature than the 1860 K of Figure 4.14. At 3 bar, their k = $200s^{-1}$ flame temperature is 1870 K, and extrapolating that line could have a slightly lower temperature at k = $400s^{-1}$. In comparison to Figure 4.14, the temperature difference for k = $200s^{-1}$ at 3 bar is about 22 K, which is considerable for two simulations that employ the same mechanism (GRI3.0). The differences between the data could be a result of how the modified OPPDIFF [56] and in-house code [7] calculate tubular flames at higher pressure. Unfortunately, the lack of higher pressure (5 bar) data from their analysis leaves the question of whether the temperature increases further or decreases slightly similar to Figure 4.14. Regardless, their results and Figure 4.14 indicate that the increase of temperature from 1 bar to 3 bar is a result of preferential diffusion.

4.2.4 Chemical Equilibrium Comparison

Even though, chemical equilibrium assumes infinitely fast reaction rates, its assumptions represent an exact thermodynamic limit. Tables 4.1-4.3 are all previous comparisons of the flame temperatures and species compositions to chemical equilibrium. The data presented from chemical equilibrium is from the solution of an adiabatic temperature and composition at constant pressure. The initial temperature of the reactants in the equilibrium software are 300 K. All species are listed in terms of mole fractions. Chemical equilibrium predicts a small temperature rise (1K) due to enhancement from pressure. This is the adiabatic flame temperature which neglects any heat transfer, incomplete combustion, and dissociation based on a certain reactant composition. All the differences in chemical equilibrium mole fraction are from one to ten orders of magnitude, especially for methane (CH_4) and the methyl (CH_3) radical. These discrepancies are largely due to the solver assuming infinitely fast reaction rates and without consideration for fluid mechanics, which is seldom in combustion. Nevertheless, its computational simplicity allows for the prediction of the evolution of species as a function of conditions such as temperature and pressure.

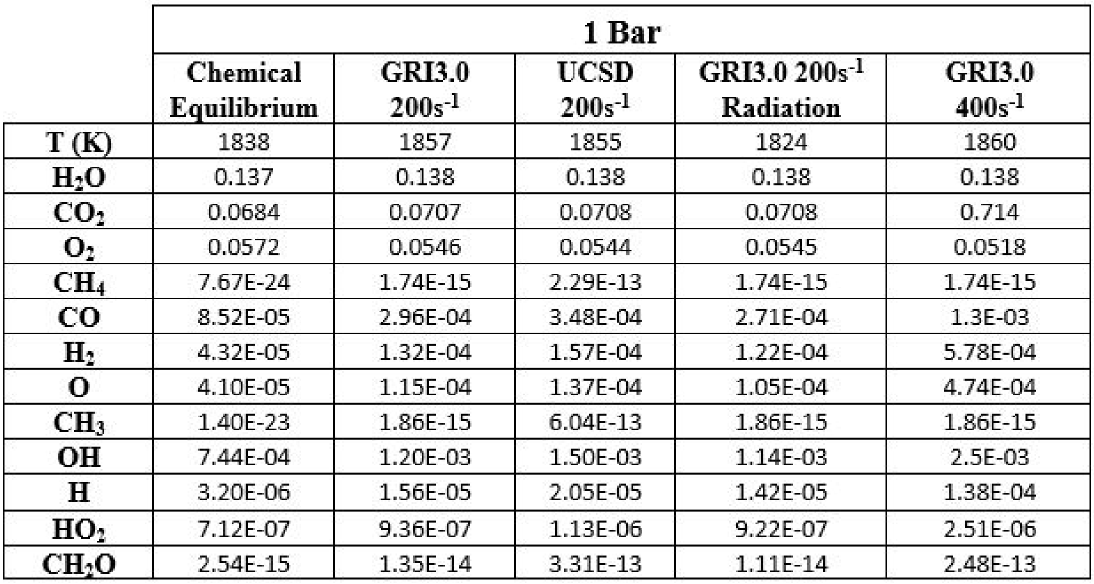

	1 Bar				
	Chemical Equilibrium	**GRI3.0 $200s^{-1}$**	**UCSD $200s^{-1}$**	**GRI3.0 $200s^{-1}$ Radiation**	**GRI3.0 $400s^{-1}$**
T (K)	1838	1857	1855	1824	1860
H_2O	0.137	0.138	0.138	0.138	0.138
CO_2	0.0684	0.0707	0.0708	0.0708	0.714
O_2	0.0572	0.0546	0.0544	0.0545	0.0518
CH_4	7.67E-24	1.74E-15	2.29E-13	1.74E-15	1.74E-15
CO	8.52E-05	2.96E-04	3.48E-04	2.71E-04	1.3E-03
H_2	4.32E-05	1.32E-04	1.57E-04	1.22E-04	5.78E-04
O	4.10E-05	1.15E-04	1.37E-04	1.05E-04	4.74E-04
CH_3	1.40E-23	1.86E-15	6.04E-13	1.86E-15	1.86E-15
OH	7.44E-04	1.20E-03	1.50E-03	1.14E-03	2.5E-03
H	3.20E-06	1.56E-05	2.05E-05	1.42E-05	1.38E-04
HO_2	7.12E-07	9.36E-07	1.13E-06	9.22E-07	2.51E-06
CH_2O	2.54E-15	1.35E-14	3.31E-13	1.11E-14	2.48E-13

Table 4.1: Species composition (mole fractions) and temperature comparisons at 1 bar. The tubular burner simulation data is taken from the centerline (r = 0 mm).

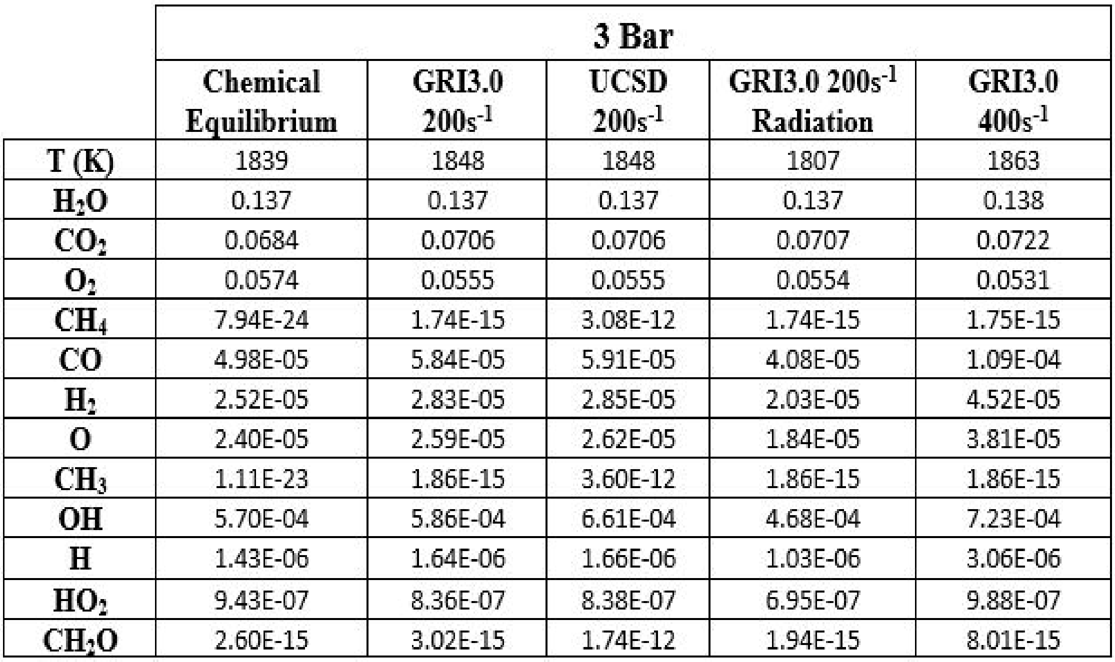

	3 Bar				
	Chemical Equilibrium	GRI3.0 $200s^{-1}$	UCSD $200s^{-1}$	GRI3.0 $200s^{-1}$ Radiation	GRI3.0 $400s^{-1}$
T (K)	1839	1848	1848	1807	1863
H_2O	0.137	0.137	0.137	0.137	0.138
CO_2	0.0684	0.0706	0.0706	0.0707	0.0722
O_2	0.0574	0.0555	0.0555	0.0554	0.0531
CH_4	7.94E-24	1.74E-15	3.08E-12	1.74E-15	1.75E-15
CO	4.98E-05	5.84E-05	5.91E-05	4.08E-05	1.09E-04
H_2	2.52E-05	2.83E-05	2.85E-05	2.03E-05	4.52E-05
O	2.40E-05	2.59E-05	2.62E-05	1.84E-05	3.81E-05
CH_3	1.11E-23	1.86E-15	3.60E-12	1.86E-15	1.86E-15
OH	5.70E-04	5.86E-04	6.61E-04	4.68E-04	7.23E-04
H	1.43E-06	1.64E-06	1.66E-06	1.03E-06	3.06E-06
HO_2	9.43E-07	8.36E-07	8.38E-07	6.95E-07	9.88E-07
CH_2O	2.60E-15	3.02E-15	1.74E-12	1.94E-15	8.01E-15

Table 4.2: Species composition (mole fractions) and temperature comparisons at 3 bar. The tubular burner simulation data is taken from the centerline (r = 0 mm).

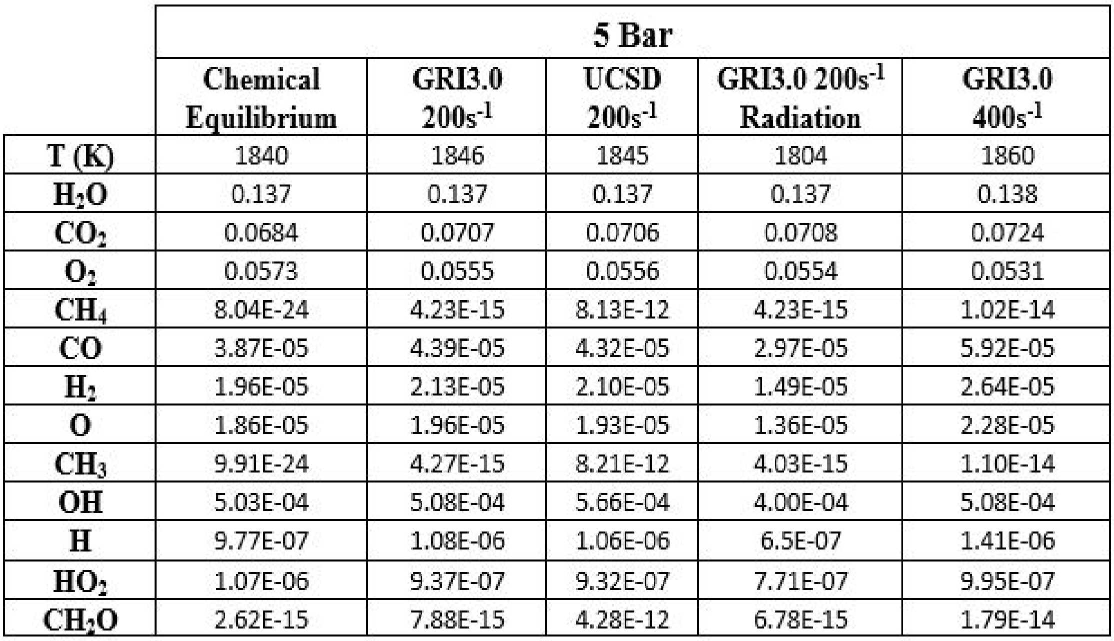

	5 Bar				
	Chemical Equilibrium	GRI3.0 $200s^{-1}$	UCSD $200s^{-1}$	GRI3.0 $200s^{-1}$ Radiation	GRI3.0 $400s^{-1}$
T (K)	1840	1846	1845	1804	1860
H_2O	0.137	0.137	0.137	0.137	0.138
CO_2	0.0684	0.0707	0.0706	0.0708	0.0724
O_2	0.0573	0.0555	0.0556	0.0554	0.0531
CH_4	8.04E-24	4.23E-15	8.13E-12	4.23E-15	1.02E-14
CO	3.87E-05	4.39E-05	4.32E-05	2.97E-05	5.92E-05
H_2	1.96E-05	2.13E-05	2.10E-05	1.49E-05	2.64E-05
O	1.86E-05	1.96E-05	1.93E-05	1.36E-05	2.28E-05
CH_3	9.91E-24	4.27E-15	8.21E-12	4.03E-15	1.10E-14
OH	5.03E-04	5.08E-04	5.66E-04	4.00E-04	5.08E-04
H	9.77E-07	1.08E-06	1.06E-06	6.5E-07	1.41E-06
HO_2	1.07E-06	9.37E-07	9.32E-07	7.71E-07	9.95E-07
CH_2O	2.62E-15	7.88E-15	4.28E-12	6.78E-15	1.79E-14

Table 4.3: Species composition (mole fractions) and temperature comparisons at 5 bar. The tubular burner simulation data is taken from the centerline (r = 0 mm).

4.2.5 Species Composition and Temperature

In equilibrium, temperatures rise and peak radicals are lower with pressure because of the completeness of third body reactions. As stated previously, the flame temperature is dependent on the completion of reactions and the residence time of the reacting species in the reaction zone. The assumption of infinitely fast reaction rates predicts reactants are being consumed and products are formed rapidly. This translates to small increases temperatures with pressure as seen in Tables 4.1-4.3.

For the tubular flame simulations using the GRI3.0 and UCSD mechanisms, at a stretch rate of $200s^{-1}$ the increasing pressure leads to a decline in temperature. This is a result of the increasing dependence of third-body reactions (like Equation 4.4) with pressure. The competition and rapid consumption of H atoms in the flame begin to impede combustion. This is why at 1 bar GRI3.0 predicts a higher temperature than UCSD as seen at the top of Table 4.1. There is also a higher peak value of H atoms located within the flame zone at 1 bar for GRI3.0 as seen in Figure 4.12. At 3 bar the profiles for GRI3.0 and UCSD are identical. At 5 bar, the temperature difference is slight as a result of lower fuel concentrations from GRI3.0 at the centerline.

The temperature differences between GRI3.0 with and without radiation of H_2O, CO_2, and CO are 33 K, 41 K, and 42 K at 1, 3, and 5 bar, respectively. Ju et al. [11] numerically computed that with radiation lean methane air flames will extinguish with increasing stretch as a result of stretch-induced incomplete combustion. The flame temperature is dependent on the time required for completion of reactions and the residence time of the reacting species. Figure 4.13 illustrates that from 1 to 3 bar the combination of radiation loss and shorter residence times (Damköhler number much less than one) causes a greater temperature loss. The tubular flame simulations predict that from 3 to 5 bar the increase in pressure has little to no effect on the amount of radiation heat loss. It is expected that if the stretch rate was increased to $400s^{-1}$ then the temperature difference due to radiation would be less. This is a result of preferential diffusion and the decreased residence time in the hot products.

The effect of stretch rate from $200s^{-1}$ to $400s^{-1}$ in Figure 4.14 and Table 4.2 show that the increase in temperature is a result of preferential diffusion. The centerline differences between 200^{-1} and $400s^{-1}$ are 3 K, 15 K, and 14 K at 1, 3, and 5 bar, respectively. From 1 to 3 bar, the nearly equidiffusive (Le $\approx$ 1) methane-air flames have a slight enhancement of mass diffusivity which show a 15K increase in temperature. In Figures 4.1 and 4.2, the convex (positively curved) shape of the wrinkles to the reactant flow is likely generating higher local values of stretch rate, flame speed, and equivalence ratios. From 3 to 5 bar, the k= $400s^{-1}$ tubular flames begins to experience a slight decrease in temperature (3K). This is a result of the Damköhler number and flame radius. At high stretch rates, the tubular flames are smaller so at high pressures the reactant species will spend less time breaking down in the reaction zone. Therefore, the preferential diffusion effects peak at 3 bar for nearly equidiffusive (Le $\approx$ 1) methane-air at k = $400s^{-1}$.

Chapter V

FUTURE WORK & SUMMARY

This work provides the framework for future investigations of high-pressure tubular flames. There are several opportunities arising from this work that should pursued to understand more about tubular flames at elevated conditions.

Further experimental investigations are necessary to capture quantitative measurements of premixed flame structure and composition. A variety of fuel and oxidizer mixtures, diluents, stretch rates, and equivalence ratios should be explored through different experimental methods. Also, non-premixed and partially premixed tubular flames should be examined and compared to know how these configurations behave in a high-pressure environment.

Likewise, additional numerical investigations would be highly beneficial. These studies should focus on the accuracy of other chemical mechanisms with variation in stretch, radiation schemes, and equivalence ratios. Two-dimensional simulations should be developed for flame cases to determine their accuracy of their 2D structure when compared to the chemiluminescence of the images as a function of pressure. Lastly, the refinement of the nonzero stretch boundary condition should be explored to determine the best scale when increasing with pressure.

Chapter VI

CONCLUSIONS

This work has been conducted to two ends: 1) to further expand knowledge on premixed methane air tubular flame response to elevated pressure, and 2) to compare simulations with previous findings on tubular flame radius, thickness, temperature, and species concentrations.

To meet the first goal, chemiluminescent images of tubular flames were examined for the first time at elevated pressures. At atmospheric pressure, lean methane-air flames show instabilities in the form of wrinkling with increasing equivalence ratio. This behavior is expected as equidiffusive (Le $\approx$ 1) methane-air flames have been shown to wrinkle rather than form cells through the absence of strong thermal-diffusive effects. At higher pressures, the wrinkling effect is no longer strongly correlated to the equivalence ratio. Premixed tubular flames are convex (positively curved) to the incoming reactant flow, and on top of the Le effects, the flame wrinkles experience an enhancement of mass diffusivity from stretch and curvature. This positive curvature is also causing local stoichiometry, stretch rate, and flame speed to increase at higher pressures. However, the unsteadiness of the flame images due to the combination of crossflow from the HPCD and PIV particles make it difficult to determine more structural properties at this time.

The 1D simulated profiles in tubular flame speed, radius, and thickness have similar trends with previous data of various equivalence ratios and burner types. The decreasing trends are a result of the competition for H atoms between pressure sensitive third order reactions. However, the discrepancies between experiment and simulation for overall flame radius occur as a result of unsteady effects (rotation, asymmetry, etc.), an incorrect nonzero stretch boundary condition (W) (See Appendix A), and limiting the simulations to 1D rather than 2D.

For the comparison of tubular flame simulations with equilibrium, the temperature rise is associated with the completeness of third body reactions. The discrepancies when compared to tubular flame simulations are a result of equilibrium assuming infinitely fast reaction rates and without consideration for fluid mechanics, which is seldom in combustion.

For the comparison of tubular flame simulations using GRI3.0 and UCSD mechanisms, the temperature and species plots show good agreement. At 1 bar, GRI3.0 predicts a thicker flame as a result of higher flame speed. The estimations of both mechanisms at 3 bar are nearly identical. The 5 bar data shows a minor temperature increase for GRI3.0 as a result of lower fuel concentrations at the centerline.

For the comparison of GRI3.0 with and without radiation, the temperature differences for the radiating species are 33 K, 41 K, and 42 K at 1, 3, and 5 bar, respectively. In previous studies, the higher stretch lean methane air flames extinguish due to stretch-induced incomplete combustion. The radiation heat loss is considerable from 1 to 3 bar. The increase in pressure reduces the residence time of reactants leading to a greater temperature loss in the flame. The temperature differences between 3 and 5 bar indicate that a further increase pressure has a negligible effect on the radiation loss.

For the comparison of GRI3.0 at $200s^{-1}$ and $400s^{-1}$ stretch, the temperature increase with pressure is a result of preferential diffusion. The centerline differences between 200^{-1} and $400s^{-1}$ are 3 K, 15 K, and 14 K at 1, 3, and 5 bar, respectively. The flame speeds for k = $400\mathrm{s}^{-1}$ at 1, 3, 5 bar is 9%, 12%, 13%, respectively, higher than $200\mathrm{s}^{-1}$. The nearly equidiffusive methane air tubular flames from 1 to 3 bar at k = $400s^{-1}$ have an enhancement of local stretch rates, flame speeds, and equivalence ratios. The temperature decrease from 3 to 5 bar is a result of the Damköhler number being much less than one. At high stretch rates, the tubular flame radius is smaller, so at high pressures the reactant species will spend less time breaking down in the reaction zone. The fast fluid flow time scales accelerate the species out into the unsteady flow field. In previous simulations, the tubular flame temperatures for k = $200s^{-1}$ at 1 and 3 bar were 1865 K and 1870 K, respectively. The higher temperatures are likely a result of how the modified OPPDIF accounts for unsteady effects at elevated pressures compared to the in-house code. But one thing is certain, the increase in temperatures with increasing stretch and pressure are a a result of preferential diffusion.

Chapter VII

Appendices

A.1 Axial Velocity Gradient (W)

A critical component to numerical simulations is the accuracy of boundary conditions. Contoured nozzles produce non-zero velocity gradients at the exits as shown in opposed-jet studies [57–59]. In previous tubular flame investigations [17], changes in the axial velocity gradient at atmospheric conditions was shown to be largely translational in flame position. The variation of this parameter increased the flame radius at high values and reduced the radius at low values. High-pressure simulations show the same sensitivities to the W boundary condition and require further analysis.

Simulations were performed at $\phi = 0.7$ and $400s^{-1}$ with the axial velocity gradient (W) varying from 120 to $180s^{-1}$. The atmospheric condition has only a small translational effect in terms of flame position as seen in Figure A.1. The higher pressures of Figures A.2 and A.3 exhibit peak temperatures fluctuating from 5 and 8 K at 3 and 5 bar, respectively. Higher temperatures were achieved when the axial velocity gradient of $120s^{-1}$ was divided by the respective pressure. In this case, W at the nozzle boundary was $40s^{-1}$ at 3 bar and $24s^{-1}$ at 5bar leading to temperature increases of 5K and 8K, respectively. It is expected the velocity gradient scales with pressure, but the extent can only be determined with further tuning and experimental measurements. At this time, fine adjustment of mesh parameters were not made but should not be ignored. A better way to know if this effect is directly related to pressure is a mesh analysis of the simulations. The key question still remains on how this value scales with given fuel-oxidizer mixtures and pressures. The axial velocity gradient is paramount to accurate atmospheric tubular flame simulations and even more so at high-pressure.

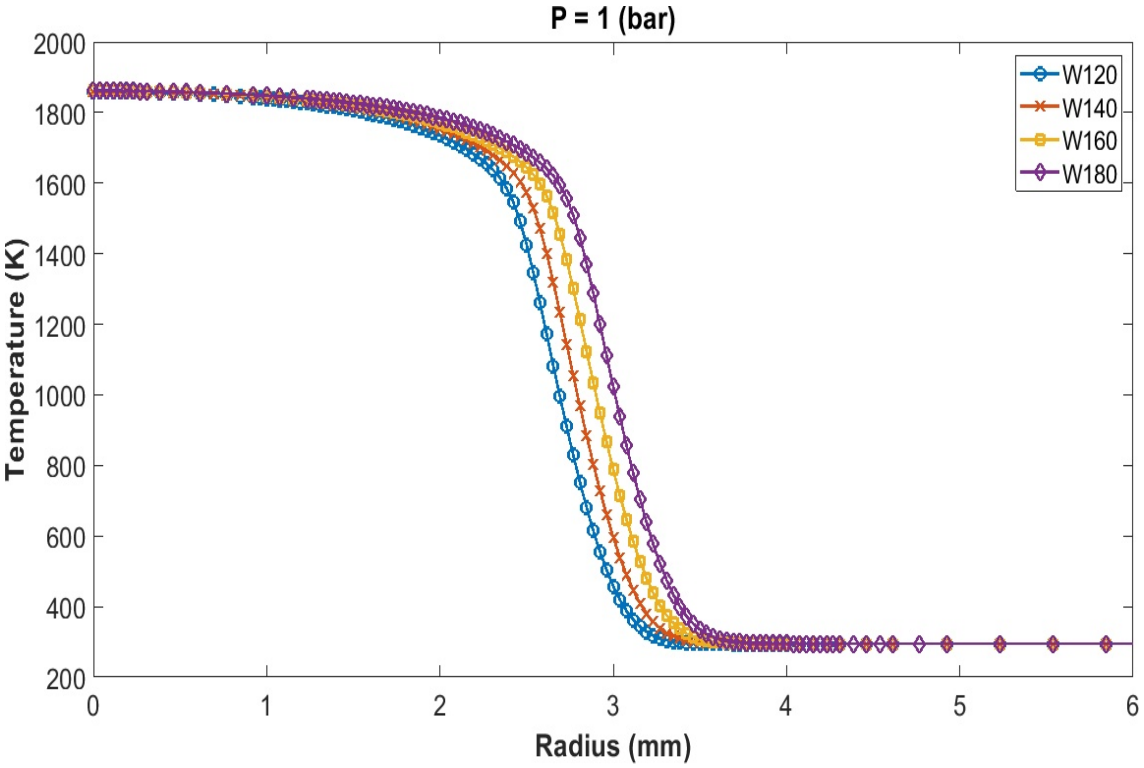

Figure A.1: Simulation temperature profiles against radial position with varying axial velocity gradient boundary condition for P = 1 bar, $\phi = 0.7$, and k = $400s^{-1}$.

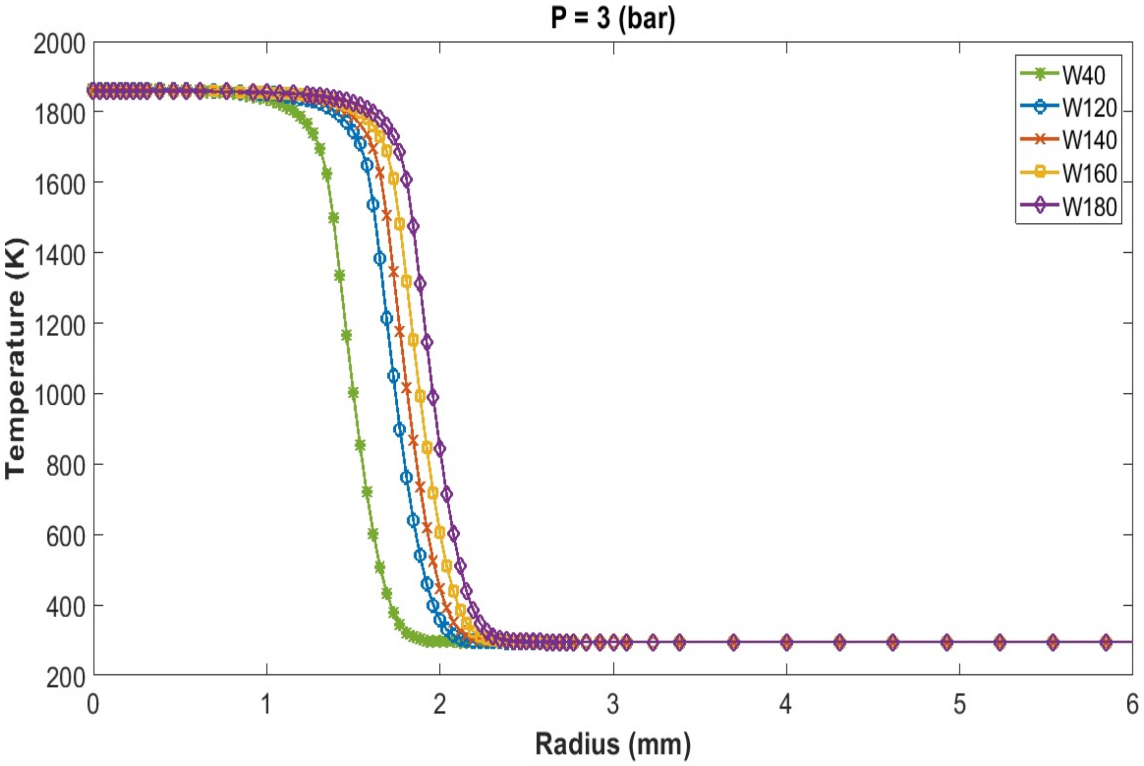

Figure A.2: Simulation temperature profiles against radial position with varying axial velocity gradient boundary condition for P = 3 bar, $\phi = 0.7$, and k = $400s^{-1}$.

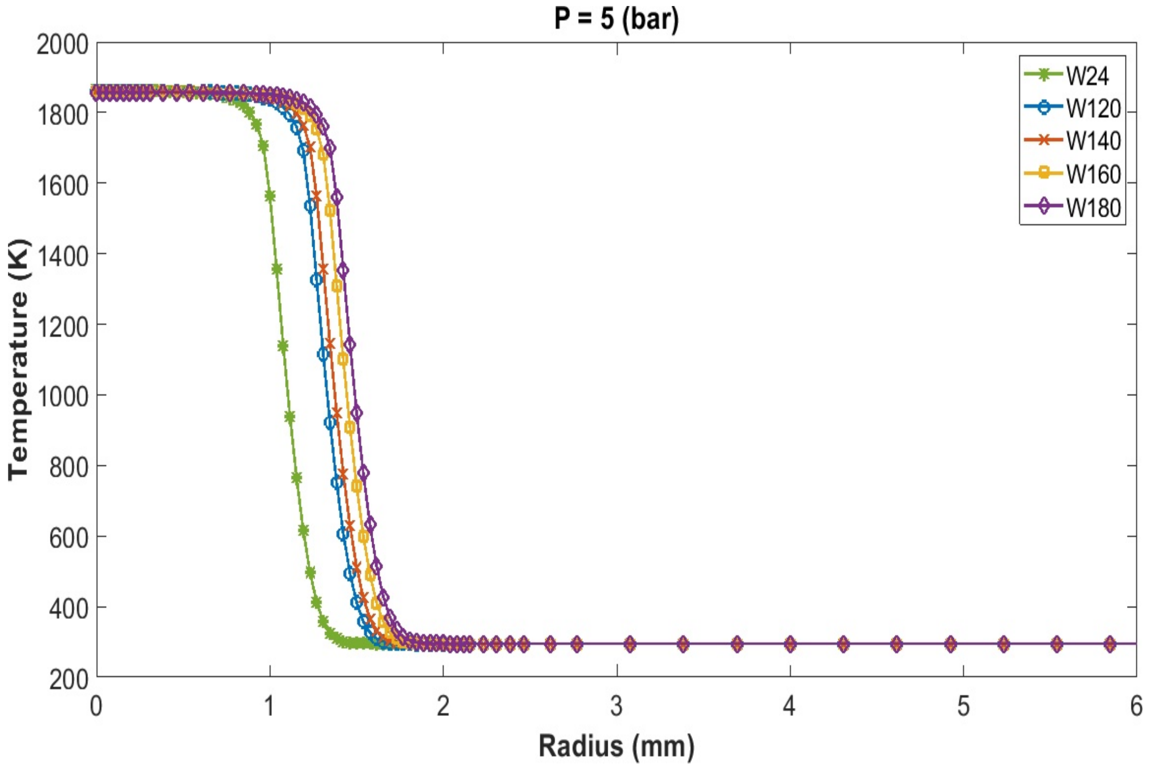

Figure A.3: Simulation temperature profiles against radial position with varying axial velocity gradient boundary condition for P = 5 bar, ϕ = 0.7, and k = $400s^{-1}$.

A.2 Radiation Comparison Species Curves (GRI3.0)

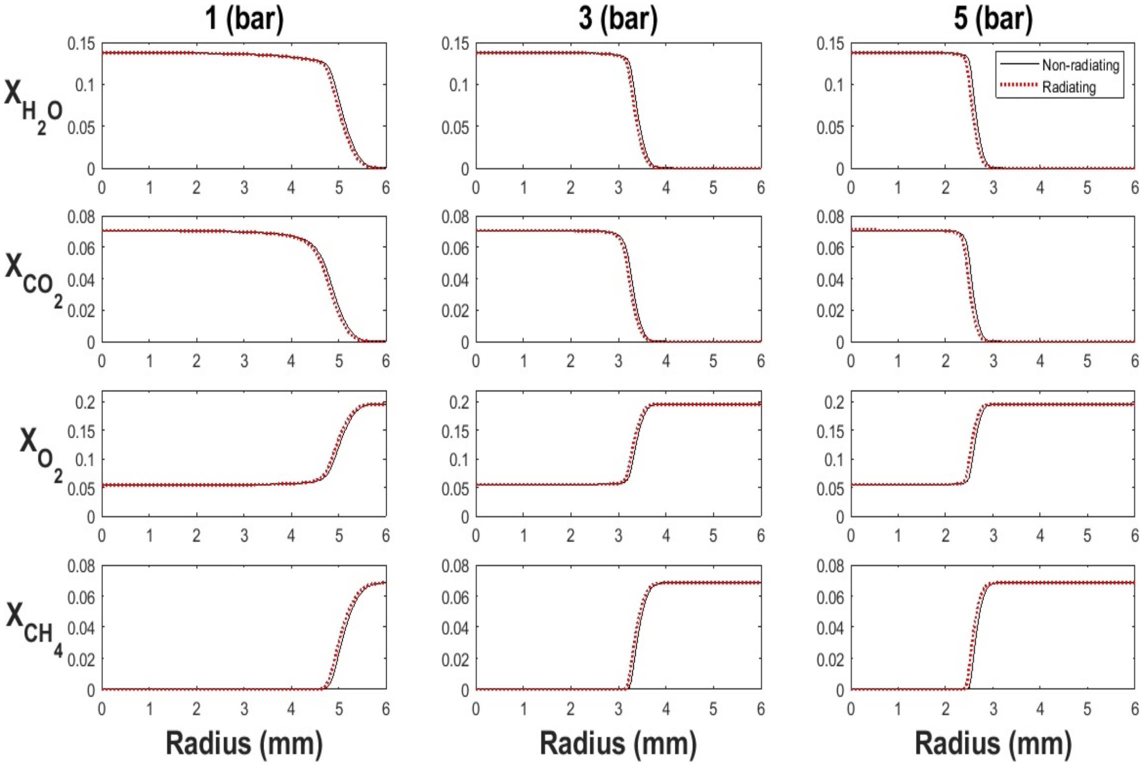

Figure A.4: Radiation comparison of flame structure for main species distributions with increasing pressure at k = 200s^{-1}.

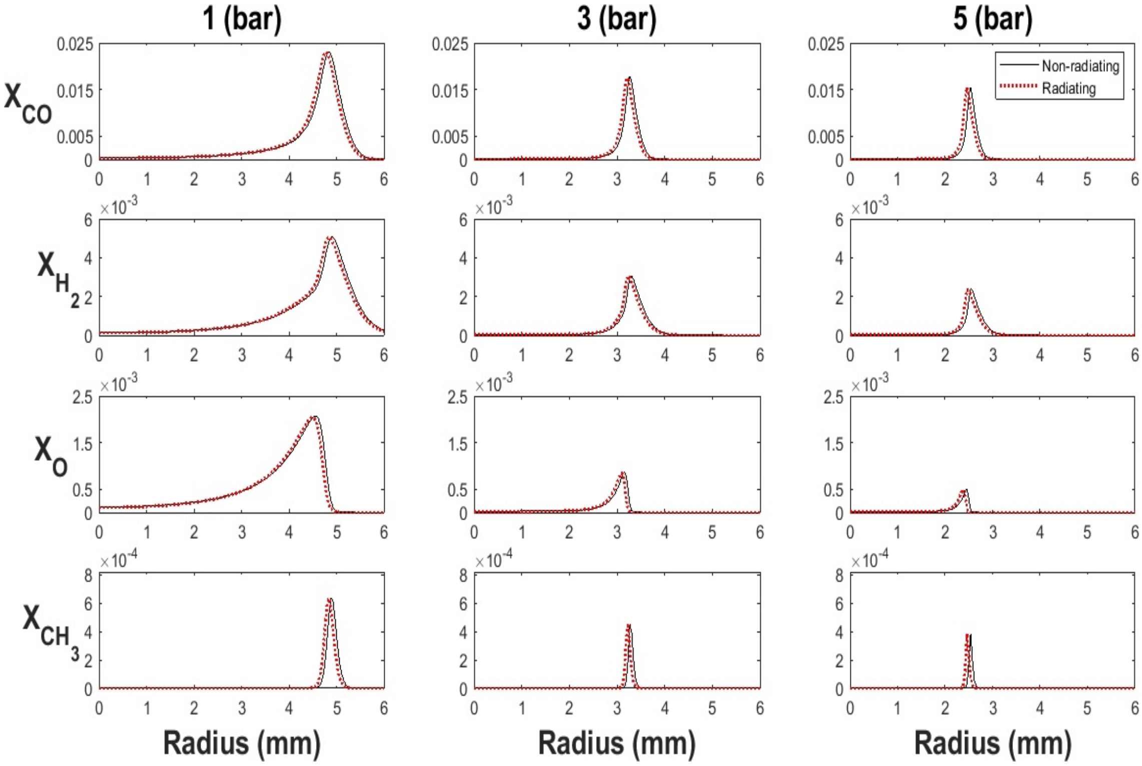

Figure A.5: Radiation comparison of flame structure for intermediate species and radicals distributions with increasing pressure at k = 200s^{-1}.

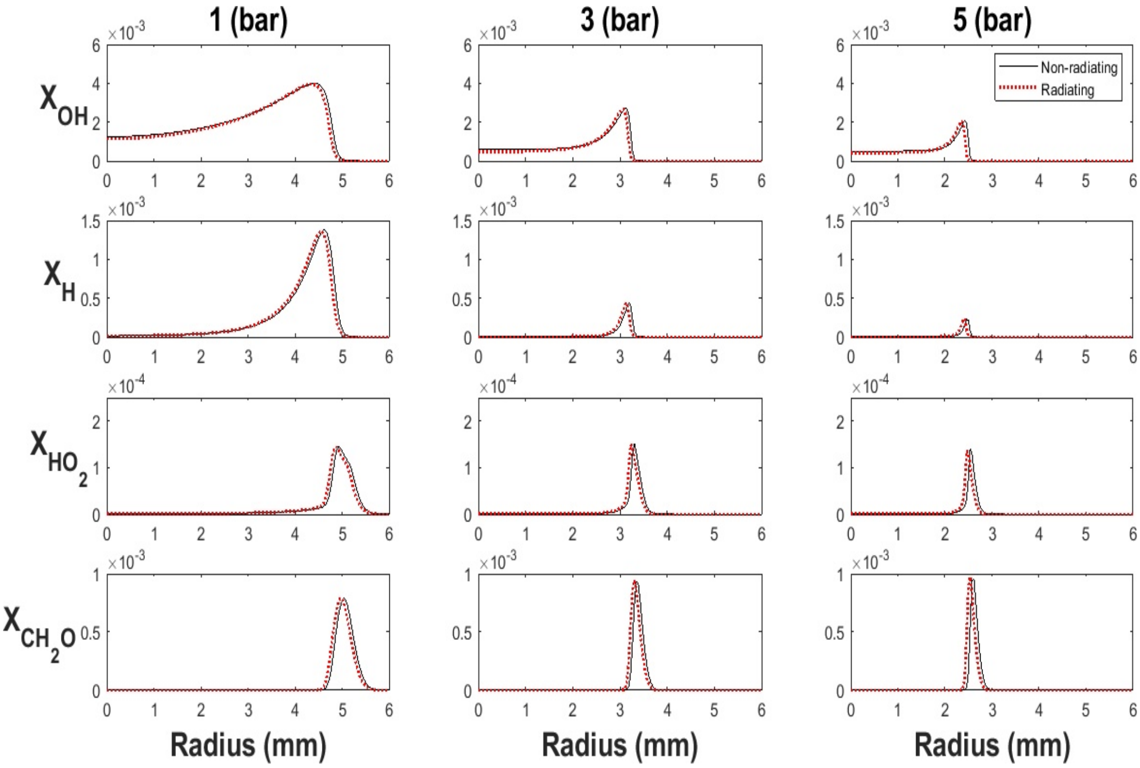

Figure A.6: Radiation comparison of flame structure for intermediate species and radicals distributions with increasing pressure at k = $200s^{-1}$.

A.3 Stretch Comparison Species Curves (GRI3.0)

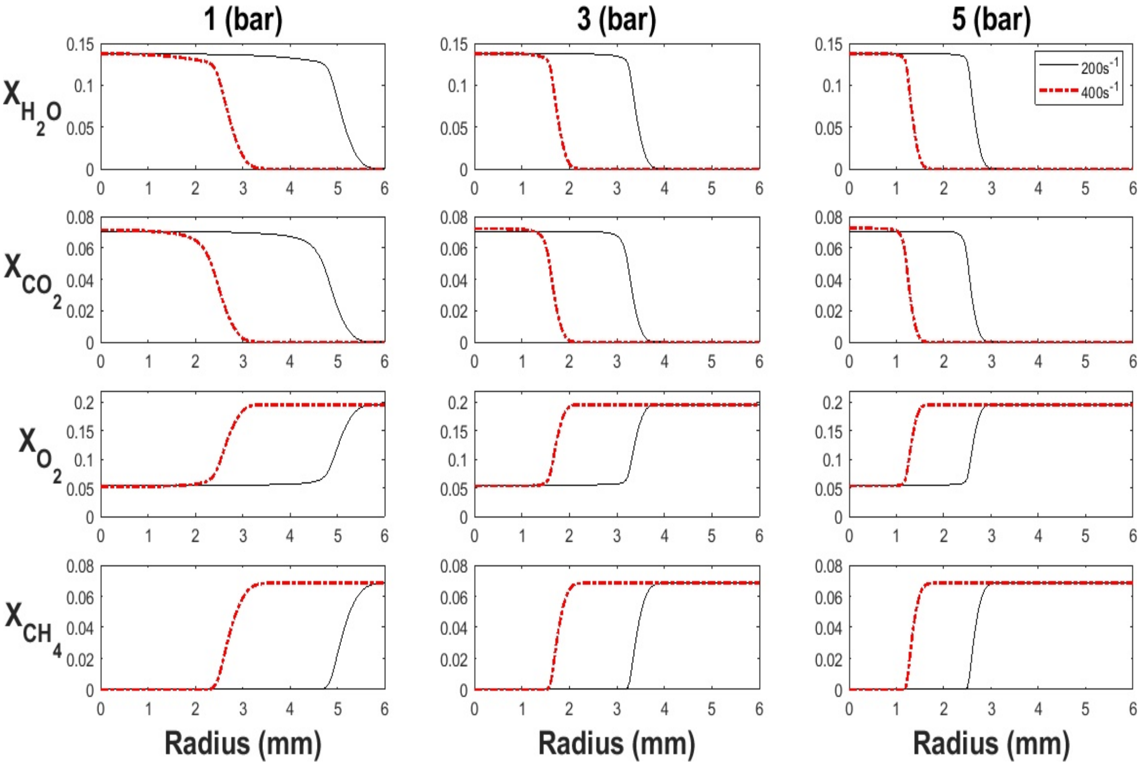

Figure A.7: Stretch comparison of flame structure for main species distributions with increasing pressure.

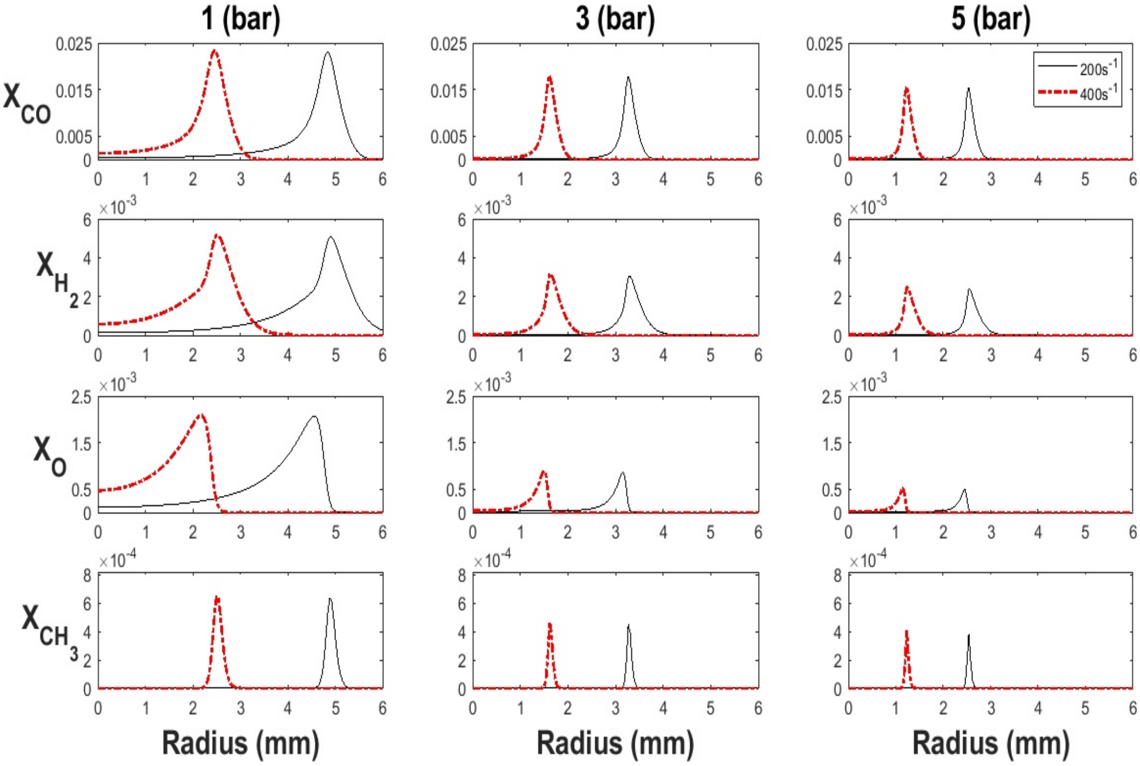

Figure A.8: Stretch comparison of flame structure for intermediate species and radicals distributions with increasing pressure.

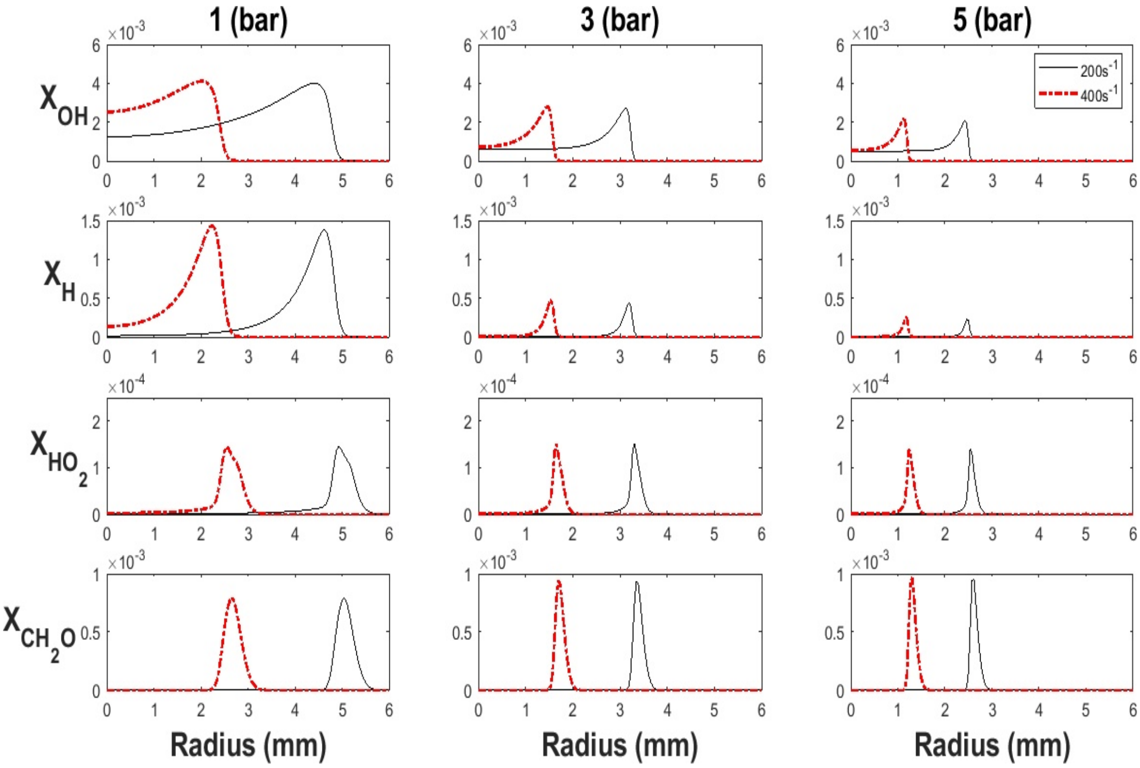

Figure A.9: Stretch comparison of flame structure for intermediate species and radicals distributions with increasing pressure.

REFERENCES

[1] P.A. Libby , F.A. Williams. Structure of laminar flamelets in premixed turbulent flames. *Combust. Flame* 44 (1982), 287–303.

[2] F.A. Williams. Recent Advances in Theoretical Descriptions of Turbulent Diffusion Flames. *Turbulent Mixing in Nonreactive and Reactive Flows.* Ed. by S. N. B. Murthy. Boston, MA: Springer, 1975, 189–208.

[3] N. Peters. Laminar flamelet concepts in turbulent combustion. *Symposium (International) on Combustion* 21 (1988), 1231–1250.

[4] D. Trees, T.M. Brown, K. Seshadri, M. D. Smooke, G. Balakrishnan, R. W. Pitz, V.Giovangigli, S. P. Nandula. The structure of nonpremixed hydrogen-air flames. *Combust. Science and Technology* 104 (1995), 427–439.

[5] D.M. Mosbacher, J.A. Wehrmeyer, R.W. Pitz, C.J. Sung, J.L. Byrd. Experimental and numerical investigation of premixed tubular flames. *Proc. Combust. Inst.* 29 (2002), 1479–1486.

[6] T. Neill, D. Judd, E. Veith, D. Rousar. Practical uses of liquid methane in rocket engine applications. *Acta Astronautica* 65 (2009), 696–705.

[7] Carl A. Hall, Robert W. Pitz. Numerical simulation of premixed H_2–air cellular tubular flames. *Combust. Theory and Modelling* 20 (2016), 328–348.

[8] B. Karlovitz, D.W. Denniston Jr., D.H. Knapschaefer, F.E. Wells. Studies on turbulent flames. *Proc. Combust. Inst.* 4 (1953), 60–68, 613–620.

[9] P.Wang, J.A. Wehrmeyer, R.W. Pitz. Stretch rate of tubular premixed flame. *Combust. Flame* 145 (2006), 401–414.

[10] F.A. Williams. “A review of some theoretical considerations of turbulent flame structure”. *AGARD Conference Proceedings no.164.* Paris, 1975, 1–25.

[11] Yiguang Ju, Hiroshi Matsumi, Kenichi Takita, Goro Masuya. Combined effects of radiation, flame curvature, and stretch on the extinction and bifurcations of cylindrical CH_4/air premixed flame. *Combust. Flame* 116 (1999), 580–592.

[12] Robert W. Pitz, Shengteng Hu, Peiyong Wang. Tubular premixed and diffusion flames: effect of stretch and curvature. *Progress in Energy and Combustion Science* 42 (2014), 1–34.

[13] M. Matalon. Intrinsic flame instabilities in premixed and nonpremixed combustion. *Annual Review of Fluid Mechanics* 39 (2007), 163–191.

[14] Yu Wang, Shengteng Hu, Robert W. Pitz. Extinction and cellular instability of premixed tubular flames. *Proc. Combust. Inst.* 32 (2009), 1141–1147.

[15] Shengteng Hu, Robert W. Pitz. Structural study of non-premixed tubular hydrocarbon flames. *Combust. Flame* 156 (2009), 51–61.

[16] Scott W. Shopoff, Peiyong Wang, Robert W. Pitz. Experimental study of cellular instability and extinction of non-premixed opposed-flow tubular flames. *Combust. Flame* 158 (2011), 2165–2177.

[17] Darren C. Tinker, Carl A. Hall, Robert W. Pitz. Measurement and simulation of partially-premixed cellular tubular flames. *Combust. Flame* 37 (2019), 2021–2028.

[18] M.Nishioka, K. Inagaki, S. Ishizuka, T. Takeno. Effects of pressure on structure and extinction of tubular flame. *Combust. Flame* 86 (1991), 90–100.

[19] Irvin Glassman, Richard A. Yetter, Nick G. Glumac. *Combustion,5th edition.* Waltham, MA: Academic Press, 2015.

[20] Yuyin Zhang, Satoru Ishizuka, Huayang Zhu, Robert J. Kee. Effects of stretch and pressure on the characteristics of premixed swirling tubular methane-air flames. *Combust. Flame* 32 (2009), 1149–1157.

[21] Campbell D. Carter, Galen B. King, Normand M. Laurendeau. Laser-induced fluorescence measurements of OH in laminar $C_2H_6/O_2/N_2$ flames at high pressure. *Combust. Sci. and Tech.* 71 (1990), 263–273.

[22] R.V. Ravikrishna, Sameer V. Naik, C.S. Cooper, Normand M. Laurendeau. Quantitative laser-induced fluorescence measurements and modeling of nitric oxide in high-pressure (6-15 atm) counterflow diffusion flames. *Combust. Sci. and Tech.* 176 (2004), 1–21.

[23] A. Matynia, M. Idir, J. Molet, C. Roche, S. de Persis, L. Pillier. Absolute OH concentration profiles measurements in high pressure counterflow flames by coupling LIF, PLIF, and absorption techniques. *Applied Physics B.* 108 (2012), 393–405.

[24] A. Matynia, M. Idir, J. Molet, C. Roche, S. de Persis, L. Pillier. Measurement of OH concentration profiles by laser diagnostics and modeling in high-pressure counterflow premixed methane/air and biogas/air flames. *Combust. Flame* 159 (2012), 3300–3311.

[25] A. Matynia, M. Idir, J. Molet, C. Roche, S. de Persis. Experimental study and modelling of NOx formation in high pressure counter-flow premixed CH_4/air flames. *Fuel* 150 (2015), 394–407.

[26] C. J. Sun, C. J. Sung, D. L. Zhu, C. K. Law. Response of counterflow premixed and diffusion flames to strain rate variations at reduced and elevated pressures. *Symposium (International) on Combustion* 26 (1996), 1111–1120.

[27] T.F. Guiberti, W.R. Boyette, W.L. Roberts, A.R. Masri. Pressure effects and transition in the stabilization mechanism of turbulent lifted flames. 37 (2019), 2167–2174.

[28] Wesley R. Boyette, Thibault F. Guiberti, Gaetano Magnotti, William L. Roberts. Structure of turbulent nonpremixed syngas flames at high pressure. 37 (2019), 2207–2214.

[29] Wesley R. Boyette, Ayman M. Elbaz, Thibault F. Guiberti, William L. Roberts. Experimental investigation of the near field in sooting turbulent nonpremixed flames at elevated pressures. *Experimental Thermal and Fluid Science* 105 (2019), 332–341.

[30] Jun Kojima, Yuji Ikeda, Tsuyoshi Nakajima. Spatially resolved measurement of OH*, CH*, and C_2* chemiluminescence in the reaction zone of laminar methane/air premixed flames. *Proc. Combust. Inst.* 28 (2000), 1757–1764.

[31] Jun Kojima, Yuji Ikeda, Tsuyoshi Nakajima. Basic aspects of OH(A), CH(A), and C_2(d) chemiluminescence in the reaction zone of laminar methane-air premixed flames. *Combust. Flame* 140 (2005), 34–45.

[32] Habib N Najm, Phillip H Paul, Charles J Mueller, Peter S Wyckoff. On the adequacy of certain experimental observables as measurements of flame burning rate. *Combust. Flame* 113 (1998), 312–332.

[33] H.N. Najm, O.M. Knio, P.H. Paul, P.S. Wyckoff. A study of flame observables in premixed methane - air flames. *Combust. Sci. and Tech.* 140 (1998), 369–403.

[34] S. Sardeshmukh, M. Bedard, W. Anderson. The use of OH* and CH* as heat release markers in combustion dynamics. *International Journal of Spray and Combustion Dynamics* 9 (2017), 409–423.

[35] J. G. Lee, D. A. Santavicca. Experimental diagnostics for the study of combustion instabilities in lean premixed combustors. *J. Prop. and Power* 19 (2003), 735–750.

[36] Holger Ax, Wolfgang Meier. Experimental investigation of the response of laminar premixed flames to equivalence ratio oscillations. *Combust. Flame* 167 (2016), 172–183.

[37] Yong Ki Jeong, Chung Hwan Jeon, Young June Chang. Evaluation of the equivalence ratio of the reacting mixture using intensity ratio of chemiluminescence in laminar partially premixed CH_4-air flames. *Experimental Thermal and Fluid Science* 30 (2006), 663–673.

[38] Venkata Nori, Jerry Seitzman. CH* chemiluminescence modeling for combustion diagnostics. *Proc. Combust. Inst.* 32 (2009), 895–903.

[39] S. A. Carl, M. Van Poppel, J. Peeters. Identification of the CH + $O_2 \rightarrow$ OH(A) + CO reaction as the source of OH(A-X) chemiluminescence in $C_2H_2/O/H/O_2$ atomic flames and determination of its absolute rate constant over the range T = 296 to 511 K. *J. Phys. Chem. A* 107 (2003), 11001–11007.

[40] Venkata Nori, Jerry Seitzman. "Evaluation of chemiluminescence as a combustion diagnostic under varying operating conditions". 46th AIAA Aerospace Sciences Meeting and Exhibit, 2008.

[41] Gregory P. Smith, Jorge Luque, Chung Park, Jay B. Jeffries, David R. Crosley. Low pressure flame determinations of rate constants for OH(A) and CH(A) chemiluminescence. *Combust. Flame* 131 (2002), 59–69.

[42] Shengteng Hu, Peiyong Wang, Robert Pitz. "A Structural Study of Premixed Tubular Flames". 44th AIAA Aerospace Sciences Meeting and Exhibit, 2006.

[43] Hermann Schlichting, Klaus Gersten, Egon Krause, Herbert Oertel, Katherine Mayes. *Boundary-Layer Theory.* Vol. 7. Springer, 1955.

[44] D. Goodwin. *Cantera: An object-oriented software toolkit for chemical kinetics, thermodynamic.* URL: `http://code.google.com/p/cantera/.`.

[45] A. Ern, V. Giovangigli. Fast and accurate multicomponent transport property evaluation. *Journal of Computational Physics* 120 (1995), 105–116.

[46] C.T. Kelley, D.E. Keyes. Convergence analysis of pseudo-transient continuation. *SIAM Journal on Numerical Analysis* 35 (1998), 508–523.

[47] Carl Hall. "Instability of Premixed Lean Hydrogen Laminar Tubular Flames". PhD thesis. Vanderbilt University, 2016.

[48] Gregory P. Smith, David M. Golden, Michael Frenklach, Nigel W. Moriarty, Boris Eiteneer, Mikhail Goldenberg, C. Thomas Bowman, Ronald K. Hanson, Soonho Song, William C. Gardiner Jr., Vitali V. Lissianski, Zhiwei Qin. URL: `http://www.me.berkeley.edu/gri_mech`.

[49] *Chemical-Kinetic Mechanisms for Combustion Applications.* URL: `http://web.eng.ucsd.edu/mae/groups/combustion/mechanism.html`.

[50] Bonnie J.McBride, Sanford Gordon. *Fortran Program for Modeling Steady Laminar One-Dimensional Premixed Flames*. NASA Reference Publication 1311. 1996.

[51] H.G. Im, C.K. Law, J.S. Kim, F.A. Williams. Response of counterflow diffusion flames to oscillating strain rates. *Combustion and Flame* 100 (1995), 21–30.

[52] R. J. Kee, J. F. Grcar, M. D. Smooke, J. A. Miller. *Fortran Program for Modeling Steady Laminar One-Dimensional Premixed Flames*. SAND85-8240. Sandia National Laboratories, 1985.

[53] Charles K. Westbrook, Frederick L. Dryer. Chemical kinetic modeling of hydrocarbon combustion. *Progress in Energy and Combustion Science* 10 (1984), 1–57.

[54] G.E. Andrews, D. Bradley. The burning velocity of methane-air mixtures. *Combustion and Flame* 19 (1972), 275–288.

[55] R.Viskanta, M.P. Menguc. Radiation heat transfer in combustion systems. *Progress in Energy and Combustion Science* 13 (1987), 97–160.

[56] A.E. Lutz, R.J. Kee, J.F. Grcar, F.M. Rupley. *OPPDIF: A Fortran Program for Computing Opposed-Flow Diffusion Flame*. SAND96-8243. Sandia National Laboratories, 1996.

[57] Jeffrey M. Bergthorson, Sean D. Salusbury, Paul E. Dimotakis. Experiments and modelling of premixed laminar stagnation flame hydrodynamics. *J. Fluid Mech.* 681 (2011), 340–369.

[58] B.G. Sarnacki, G. Esposito, R.H. Krauss, H.K. Chelliah. Extinction limits and associated uncertainties of non-premixed counterflow flames of methane, ethylene, propylene and n-butane in air. *Combust. Flame* 159 (2012), 1026–1043.

[59] Ulrich Niemann, Kalyanasundaram Seshadri, Forman A. Williams. Accuracies of laminar counterflow flame experiments. *Combust. Flame* 162 (2015), 1540–1549.